

1 **Impacts of microtopographic snow-redistribution and lateral subsurface processes**
2 **on hydrologic and thermal states in an Arctic polygonal ground ecosystem : A case**
3 **study using ELM-3D v1.0**
4

5 **Gautam Bisht¹, William J. Riley¹, Haruko M. Wainwright¹, Baptiste Dafflon¹, Yuan**
6 **Fengming², and Vladimir E. Romanovsky³**
7

8 ¹Climate & Ecosystem Sciences Division, Lawrence Berkeley National Laboratory,1
9 Cyclotron Road, Berkeley, California 94720, USA
10

11 ²Environmental Sciences Division, Oak Ridge National Laboratory, Oak Ridge, TN, 37831-
12 6301 , USA
13

14 ³Geophysical Institute, University of Alaska Fairbanks, Fairbanks, AK 99775, USA
15

16 Correspondence to: Gautam Bisht (gbisht@lbl.gov)
17

18 **Abstract**

19 Microtopographic features, such as polygonal ground, are characteristic sources of
20 landscape heterogeneity in the Alaskan Arctic coastal plain. Here, we analyze the effects of
21 snow redistribution (SR) and lateral subsurface processes on hydrologic and thermal states
22 at a polygonal tundra site near Barrow, Alaska. We extended the land model integrated in
23 the E3SM to redistribute incoming snow by accounting for microtopography and
24 incorporated subsurface lateral transport of water and energy (ELM-3D v1.0). Multiple 10-
25 years long simulations were performed for a transect across polygonal tundra landscape at
26 the Barrow Environmental Observatory in Alaska to isolate the impact of SR and
27 subsurface process representation. When SR was included, model predictions better
28 agreed (higher R^2 , lower bias and RMSE) with observed differences in snow depth between
29 polygonal rims and centers. The model was also able to accurately reproduce observed soil
30 temperature vertical profiles in the polygon rims and centers (overall bias, RMSE, and R^2 of
31 0.59°C , 1.82°C , and 0.99, respectively). The spatial heterogeneity of snow depth during the

32 winter due to SR generated surface soil temperature heterogeneity that propagated in
33 depth and time and led to ~10 cm shallower and ~5 cm deeper maximum annual thaw
34 depths under the polygon rims and centers, respectively. Additionally, SR led to spatial
35 heterogeneity in surface energy fluxes and soil moisture during the summer. Excluding
36 lateral subsurface hydrologic and thermal processes led to small effects on mean states but
37 an overestimation of spatial variability in soil moisture and soil temperature as subsurface
38 liquid pressure and thermal gradients were artificially prevented from spatially dissipating
39 over time. The effect of lateral subsurface processes on maximum thaw depths was modest,
40 with mean absolute differences of ~3 cm. Our integration of three-dimensional subsurface
41 hydrologic and thermal subsurface dynamics in the E3SM land model will facilitate a wide
42 range of analyses heretofore impossible in an ESM context.

43 **1 Introduction**

44 The northern circumpolar permafrost region, which contains ~1700 Pg of organic
45 carbon down to 3 m (Tarnocai et al., 2009), is predicted to experience disproportionately
46 larger future warming compared to the tropics and temperate latitudes (Holland and Bitz,
47 2003). Recent warming in the Arctic has led to changes in lake area (Smith et al., 2005),
48 snow cover duration and extent (Callaghan et al., 2011a), vegetation cover (Sturm et al.,
49 2005), growing season length (Smith et al., 2004), thaw depth (Schuur et al., 2008),
50 permafrost stability (Jorgenson et al., 2006), and land-atmosphere feedbacks (Euskirchen
51 et al., 2009). Future predictions of Arctic warming include northward expansion of shrub
52 cover in tundra (Sturm et al., 2001; Tape et al., 2006), decreases in snow cover duration
53 (Callaghan et al., 2011a), and emissions of CO₂ and CH₄ from decomposition of
54 belowground soil organic matter (Koven et al., 2011; Schaefer et al., 2011; Schuur and
55 Abbott, 2011; Xu et al., 2016).

56 Several recent modeling studies have predicted a positive global carbon-climate
57 feedback at the global scale (Cox et al., 2000; Dufresne et al., 2002; Friedlingstein et al.,
58 2001; Fung et al., 2005; Govindasamy et al., 2011; Jiang et al., 2011; Jones et al., 2003;
59 Koven et al., 2015; Matthews et al., 2007a; Matthews et al., 2005; Sitch et al., 2008;
60 Thompson et al., 2004; Zeng et al., 2004), although the strength of this predicted feedback

61 at the year 2100 was shown to have a large variability across models (Friedlingstein et al.,
62 2006). In contrast to the ocean carbon cycle, the terrestrial carbon cycle is expected to be a
63 more dominant factor in the global carbon-climate feedback over the next century
64 (Matthews et al., 2007b; Randerson et al., 2015).

65 Snow, which covers the Arctic ecosystem for 8-10 months each year (Callaghan et
66 al., 2011b), is a critical factor influencing hydrologic and ecologic interactions (Jones,
67 1999). Snowpack modifies surface energy balances (via high reflectivity), soil thermal
68 regimes (due to low thermal conductivity), and hydrologic cycles (because of melt water).
69 Several studies have shown that warm soil temperatures under snowpack support the
70 emission of greenhouse gases from belowground respiration (Grogan and Chapin Iii, 1999;
71 Sullivan, 2010) and nitrogen mineralization (Borner et al., 2008; Schimel et al., 2004)
72 during winter. Additionally, decreases in snow cover duration have been shown to increase
73 net ecosystem CO₂ uptake (Galen and Stanton, 1995; Groendahl et al., 2007). Recent snow
74 manipulation experiments in the Arctic have provided evidence of the importance of snow
75 in the expected responses of Arctic ecosystems under future climate change (Morgner et al.,
76 2010; Nobrega and Grogan, 2007; Rogers et al., 2011; Schimel et al., 2004; Wahren et al.,
77 2005; Welker et al., 2000).

78 Apart from the spatial extent and duration of snowpack, the spatial heterogeneity of
79 snow depth is an important factor in various terrestrial processes (Clark et al., 2011;
80 Lundquist and Dettinger, 2005). As synthesized by López-Moreno et al. (2014), the
81 following processes are responsible for snow depth heterogeneity at three distinct spatial
82 scales: microtopography at 1-10 m (Lopez-Moreno et al., 2011); wind induced lateral
83 transport processes at 100-1000 m (Liston et al., 2007); and precipitation variability at
84 catchment scales of 10 – 1000 km (Sexstone and Fassnacht, 2014). The spatial distribution
85 of snow not only affects the quantity of snowmelt discharge (Hartman et al., 1999; Luce et
86 al., 1998), but also the water chemistry (Rohrbough et al., 2003; Wadham et al., 2006;
87 Williams et al., 2001). Lawrence and Swenson (2011) demonstrated the importance of
88 snow depth heterogeneity in predicting responses of the Arctic ecosystem to future climate
89 change by performing idealized numerical simulations of shrub expansion across the pan-
90 Arctic region using the Community Land Model (CLM4). Their results showed that an
91 increase in active layer thickness (ALT), which is the maximum annual thaw depth, under

92 shrubs was negated when spatial heterogeneity in snow cover due to wind driven snow
93 redistribution was accounted for, resulting in an unchanged grid cell mean active layer
94 thickness.

95 Large portions of the Arctic are characterized by polygonal ground features, which
96 are formed in permafrost soil when frozen ground cracks due to thermal contraction
97 during winter and ice wedges form within the upper several meters (Hinkel et al., 2005).
98 Polygons can be classified as 'low-centered' or 'high-centered' based on the relationship
99 between their central and mean elevations. Polygonal ground features are dynamic
100 components of the Arctic landscape in which the upper part of ice-wedge thaw under low-
101 centered polygon troughs leads to subsidence, eventually (~o(centuries)) converting the
102 low-centered polygon into a high-centered polygon (Seppala et al., 1991). Microtopography
103 of polygonal ground influences soil hydrologic and thermal conditions (Engstrom et al.,
104 2005). In addition to controlling CO₂ and CH₄ emissions, soil moisture affects (1)
105 partitioning of incoming radiation into latent, sensible, and ground heat fluxes (Hinzman
106 and Kane, 1992; McFadden et al., 1998); (2) photosynthesis rates (McGuire et al., 2000;
107 Oberbauer et al., 1991; Oechel et al., 1993; Zona et al., 2011); and (3) vegetation
108 distributions (Wiggins, 1951).

109 Our goals in this study include (1) analyzing the effects of spatially heterogeneous
110 snow in polygonal ground on soil temperature and moisture and surface processes (e.g.,
111 surface energy budgets); (2) analyzing how model predictions are affected by inclusion of
112 lateral subsurface hydrologic and thermal processes; and (3) developing and testing a
113 three-dimensional version of the E3SM Land Model (ELM; (Tang and Riley, 2016; Zhu and
114 Riley, 2015)), called ELM-3D v1.0 (hereafter ELM-3D). We then applied ELM-3D to a
115 transect across a polygonal tundra landscape at the Barrow Environmental Observatory in
116 Alaska. After defining our study site, the model improvements, model tests against
117 observations, and analyses, we apply the model to examine the effects of snow
118 redistribution and lateral subsurface processes on snow micro-topographical
119 heterogeneity, soil temperature, and the surface energy budget.

120 **2 Methodology**

121 **2.1 Study Area**

122 Our analysis focuses on sites located near Barrow, Alaska (71.3° N, 156.5° W) from
123 the long term Department of Energy (DOE) Next-Generation Ecosystem Experiment (NGEE-
124 Arctic) project. The four primary NGEE-Arctic study sites (A, B, C, D) are located within the
125 Barrow Environmental Observatory (BEO), which is situated on the Alaskan Coastal Plain.
126 The annual mean air temperature for our study sites is approximately -13°C (Walker et al.,
127 2005) and mean annual precipitation is 106 mm with the majority of precipitation
128 occurring during the summer season (Wu et al., 2013). The study site is underlain with
129 continuous permafrost (Brown et al., 1980) and the annual maximum thaw depth (active
130 layer depth) ranges between 30-90 cm (Hinkel et al., 2003). Although the overall
131 topographic relief for the BEO is low, the four NGEE study sites have distinct
132 microtopographic features: low-centered (A), high-centered (B), and transitional polygons
133 (C, D). Contrasting polygon types are indicative of different stages of permafrost
134 degradation and were the primary motivation behind the choice of study sites for the
135 NGEE-Arctic project. LIDAR Digital Elevation Model (DEM) data were available at 0.25 m
136 resolution for the region encompassing all four NGEE sites. In this work, we perform
137 simulations along a two-dimensional transect in low-centered polygon Site-A as shown by
138 the dotted line in Figure 1.

139 **2.2 ELMv0 Description**

140 The original version of ELM is equivalent to CLM4.5 (Ghimire et al., 2016; Koven et
141 al., 2013; Oleson, 2013a), and represents vertical energy and water dynamics, including
142 phase change. We developed ELM-3D by expanding on that model to explicitly represent
143 soil lateral energy and hydrological exchanges and fine-resolution snow redistribution. We
144 run ELM-3D here with prescribed plant phenology (called Satellite Phenology (SP) mode),
145 since our focus is on thermal dynamics of the system, rather than C cycle dynamics.

146 2.3 Representing Two- and Three-Dimensional Physics

147 2.3.1 Subsurface hydrology

148 The flow of water in the unsaturated zone is given by the θ -based Richards
149 equations as

$$\frac{\partial \theta}{\partial t} = -\nabla \cdot \vec{q} - Q \quad (1)$$

150 where θ [m^3m^{-3}] is the volumetric soil water content, t [s] is time, \vec{q} [m s^{-1}] is Darcy flux, and
151 Q [m^{-3} of water m^{-3} of soil s^{-1}] is volumetric sink of water. Darcy flux is given by

$$\vec{q} = -k\nabla(\psi + z) \quad (2)$$

152 where k [m s^{-1}] is the hydraulic conductivity, ψ [m] is the soil matric potential, and z [m] is
153 height above a reference datum. The hydraulic conductivity and soil matric potential are
154 non-linear functions of volumetric soil moisture. ELMv0 uses the modified form of Richards
155 equation of Zeng and Decker (2009) that computes Darcy flux as

$$\vec{q} = -k\nabla(\psi + z - C) \quad (3)$$

156 where C is a constant hydraulic potential above the water table, z_{∇} , given as

$$C = \psi_E + z = \psi_{sat} \left[\frac{\theta_E(z)}{\theta_{sat}} \right]^{-B} + z = \psi_{sat} + z_{\nabla} \quad (4)$$

157 where ψ_E [m] is the equilibrium soil matric potential, ψ_{sat} [m] is the saturated soil matric
158 potential, θ_E [$\text{m}^3 \text{m}^{-3}$] is volumetric soil water content at equilibrium soil matric potential,
159 θ_{sat} [$\text{m}^3 \text{m}^{-3}$] is volumetric soil water content at saturation, z_{∇} [m] is height of water table
160 above the reference datum, and B [-] is a fitting parameter for soil-water characteristic
161 curves. Substituting equations (3) and (4) into equation (1) yields the equation for the
162 vertical transport of water in ELMv0:

$$\frac{\partial \theta}{\partial t} = \frac{\partial}{\partial z} \left[k \left(\frac{\partial(\psi - \psi_E)}{\partial z} \right) \right] - Q \quad (5)$$

163 A finite volume spatial discretization and implicit temporal discretization with Taylor
164 series expansion leads to a tri-diagonal system of equations. We extended this 1-D Richards
165 equation to a 3-D representation integrated in ELM-3D, which is presented next.

166 We use a cell-centered finite volume discretization to decompose the spatial domain
167 into N non-overlapping control volumes, Ω_n , such that $\Omega = \bigcup_{n=1}^N \Omega_n$ and Γ_n represents the

168 boundary of the n -th control volume. Applying a finite volume integral to equation (1) and
 169 the divergence theorem yields

$$\frac{\partial}{\partial t} \int_{\Omega_n} \theta dV = - \int_{\Gamma_n} (\vec{q} \cdot d\vec{A}) - \int_{\Omega_n} Q dV \quad (6)$$

170 The spatially discretized equation for the n -th grid cell that has V_n volume and n' neighbors
 171 is given by

$$\frac{d\theta_n}{dt} V_n = - \sum_{n'} (\vec{q}_{nn'} \cdot \vec{A}_{nn'}) - Q V_n \quad (7)$$

172 For the sake of simplicity in presenting the discretized equation, we assume the 3-D grid is
 173 a Cartesian grid with each grid cell having a thickness of Δx , Δy , and Δz in the x , y , and z
 174 directions, respectively. Using an implicit time integral, the 3-D discretized equation at time
 175 $t + 1$ for a (i, j, k) control volume is given as

$$\begin{aligned} \left(\frac{\Delta\theta_{i,j,k}^{t+1}}{\Delta t} \right) V_{i,j,k} = & \left(q_{x_{i-1/2,j,k}}^{t+1} - q_{x_{i+1/2,j,k}}^{t+1} \right) \Delta y \Delta z \\ & + \left(q_{y_{i,j-1/2,k}}^{t+1} - q_{y_{i,j+1/2,k}}^{t+1} \right) \Delta x \Delta z \\ & + \left(q_{z_{i,j,k-1/2}}^{t+1} - q_{z_{i,j,k+1/2}}^{t+1} \right) \Delta x \Delta y - Q V_{i,j,k} \end{aligned} \quad (8)$$

176 where q_x , q_y and q_z are Darcy flux in the x , y , and z directions, respectively and $\Delta\theta_{i,j,k}^{t+1}$ is the
 177 change in volumetric soil liquid water in time Δt . Using the same approach as Oleson
 178 (2013b), the Darcy flux in all three directions is linearized about θ using Taylor series
 179 expansion. The linearized Darcy flux in the x direction at the $(i - 1/2, j, k)$ interface is a
 180 function of $\theta_{i-1,j,k}$ and $\theta_{i,j,k}$:

$$q_{x_{i-1/2,j,k}}^{t+1} = q_{x_{i-1/2,j,k}}^t + \frac{\partial q_{x_{i-1/2,j,k}}^t}{\partial \theta_{i-1,j,k}} \Delta\theta_{i-1,j,k}^{t+1} + \frac{\partial q_{x_{i-1/2,j,k}}^t}{\partial \theta_{i,j,k}} \Delta\theta_{i,j,k}^{t+1} \quad (9)$$

181 The linearized Darcy fluxes in the y and z directions are computed similarly. Substituting
 182 equation (9) in equation (8) results in a banded matrix of the form

$$\begin{aligned} \alpha \Delta\theta_{i-1,j,k}^{t+1} + \beta \Delta\theta_{i,j-1,k}^{t+1} + \gamma \Delta\theta_{i,j,k-1}^{t+1} + \eta \Delta\theta_{i+1,j,k}^{t+1} + \mu \Delta\theta_{i,j+1,k}^{t+1} + \phi \Delta\theta_{i,j,k+1}^{t+1} \\ + \zeta \Delta\theta_{i,j,k}^{t+1} = \varphi \end{aligned} \quad (10)$$

183 where α , β , and γ are subdiagonal entries; η , μ , and ϕ are superdiagonal entries; ζ is
 184 diagonal entry of the banded matrix is given by

$$\alpha = \frac{\partial q_{x_{i-1/2,j,k}}^t}{\partial \theta_{i-1,j,k}} \Delta y \Delta z \quad (11)$$

$$\beta = \frac{\partial q_{y_{i,j-1/2,k}}^t}{\partial \theta_{i,j-1,k}} \Delta x \Delta z \quad (12)$$

$$\gamma = \frac{\partial q_{z_{i,j,k-1/2}}^t}{\partial \theta_{i,j,k-1}} \Delta x \Delta y \quad (13)$$

$$\eta = \frac{\partial q_{x_{i+1/2,j,k}}^t}{\partial \theta_{i+1,j,k}} \Delta y \Delta z \quad (14)$$

$$\mu = \frac{\partial q_{y_{i,j+1/2,k}}^t}{\partial \theta_{i,j+1,k}} \Delta x \Delta z \quad (15)$$

$$\phi = \frac{\partial q_{z_{i,j,k+1/2}}^t}{\partial \theta_{i,j,k+1}} \Delta x \Delta y \quad (16)$$

$$\begin{aligned} \zeta = & \left(\frac{\partial q_{x_{i-1/2,j,k}}^t}{\partial \theta_{i,j,k}} - \frac{\partial q_{x_{i+1/2,j,k}}^t}{\partial \theta_{i,j,k}} \right) \Delta y \Delta z + \left(\frac{\partial q_{y_{i,j-1/2,k}}^t}{\partial \theta_{i,j,k}} - \frac{\partial q_{y_{i,j+1/2,k}}^t}{\partial \theta_{i,j,k}} \right) \Delta x \Delta z \quad (17) \\ & + \left(\frac{\partial q_{z_{i,j,k-1/2}}^t}{\partial \theta_{i,j,k}} - \frac{\partial q_{z_{i,j,k+1/2}}^t}{\partial \theta_{i,j,k}} \right) \Delta x \Delta y - \frac{\Delta x \Delta x \Delta z}{\Delta t} \end{aligned}$$

185

186 The column vector φ is given by

$$\begin{aligned} \varphi = & - \left(q_{x_{i-1/2,j,k}}^t - q_{x_{i+1/2,j,k}}^t \right) \Delta y \Delta z - \left(q_{y_{i,j-1/2,k}}^t - q_{y_{i,j+1/2,k}}^t \right) \Delta x \Delta z \quad (18) \\ & - \left(q_{z_{i,j,k-1/2}}^t - q_{z_{i,j,k+1/2}}^t \right) \Delta x \Delta y + Q_{i,j,k}^{t+1} \Delta x \Delta x \Delta z \end{aligned}$$

187

188 The coefficients of equation (10) described in equation (11)-(18) are for an internal grid
 189 cell with six neighbors. The coefficients for the top and bottom grid cells are modified for
 190 infiltration and interaction with the unconfined aquifer in the same manner as Oleson
 191 (2013b). Similarly, the coefficients for the grid cells on the lateral boundary are modified
 192 for a no-flux boundary condition. See Oleson (2013b) for details about the computation of
 193 hydraulic properties and derivative of Darcy flux with respect to soil liquid water content.

194 **2.3.2 Subsurface thermal**

195 ELMv0 solves a tightly coupled system of equations for soil, snow, and standing
 196 water temperature (Oleson, 2013a). The model solves the transient conservation of energy:

$$c \frac{\partial T}{\partial t} = -\nabla \cdot \mathbf{F} \quad (19)$$

197 where c is the volumetric heat capacity [$\text{J m}^{-3} \text{K}^{-1}$], \mathbf{F} is the heat flux [W m^{-2}], and t is time
 198 [s]. The heat conduction flux is given by

$$\mathbf{F} = -\lambda \nabla T \quad (20)$$

199 where λ is thermal conductivity [$\text{W m}^{-1} \text{K}^{-1}$] and T is temperature [K]. Applying a finite
 200 volume integral to equation (20) and divergence theorem yields

$$c \frac{\partial}{\partial t} \int_{\Omega_n} T = - \int_{\Gamma_n} \vec{\mathbf{F}} \cdot d\vec{\mathbf{A}} \quad (21)$$

201 The spatially discretized equation for a n -th grid cell that has V_n volume and n' neighbors is
 202 given by

$$c_n \frac{dT_n}{dt} V_n = - \sum_{n'} (\vec{\mathbf{F}}_{nn'} \cdot \vec{\mathbf{A}}_{nn'}) \quad (22)$$

203 Similar to the approach taken in Section 2.3.1, ELM-3D assumes a 3-D Cartesian grid with
 204 each grid cell having a thickness of Δx , Δy , and Δz in the x , y , and z directions, respectively.
 205 Temporal integration of equation (22) is carried out using the Crank-Nicholson method
 206 that uses a linear combination of fluxes evaluated at time t and $t + 1$:

$$\begin{aligned} & c_{n_{i,j,k}} \frac{(T_{i,j,k}^{t+1} - T_{i,j,k}^t)}{\Delta t} \Delta x \Delta y \Delta z \\ &= \omega \left\{ \left(F_{x_{i-\frac{1}{2},j,k}}^t - F_{x_{i+\frac{1}{2},j,k}}^t \right) \Delta y \Delta z + \left(F_{y_{i,j-\frac{1}{2},k}}^t - F_{y_{i,j+\frac{1}{2},k}}^t \right) \Delta x \Delta z \right. \\ &+ \left. \left(F_{z_{i,j,k-\frac{1}{2}}}^t - F_{z_{i,j,k+\frac{1}{2}}}^t \right) \Delta x \Delta y \right\} \\ &+ (1 - \omega) \left\{ \left(F_{x_{i-\frac{1}{2},j,k}}^{t+1} - F_{x_{i+\frac{1}{2},j,k}}^{t+1} \right) \Delta y \Delta z \right. \\ &+ \left(F_{y_{i,j-\frac{1}{2},k}}^{t+1} - F_{y_{i,j+\frac{1}{2},k}}^{t+1} \right) \Delta x \Delta z \\ &+ \left. \left(F_{z_{i,j,k-\frac{1}{2}}}^{t+1} - F_{z_{i,j,k+\frac{1}{2}}}^{t+1} + 1 \right) \Delta x \Delta y \right\} \end{aligned} \quad (23)$$

207 where ω is the weight in the Crank-Nicholson method and set to 0.5 in this study.
 208 Substituting a discretized form of heat flux using equation (20) in equation (23), results in
 209 a banded matrix of the form

$$\alpha T_{i-1,j,k}^{t+1} + \beta T_{i,j-1,k}^{t+1} + \gamma T_{i,j,k-1}^{t+1} + \eta T_{i+1,j,k}^{t+1} + \mu T_{i,j+1,k}^{t+1} + \phi T_{i,j,k+1}^{t+1} + \zeta \Delta T_{i,j,k}^{t+1} = \varphi \quad (24)$$

210 where α , β , and γ are subdiagonal entries; η , μ , and ϕ are superdiagonal entries; ζ is
 211 diagonal entry of the banded matrix is given by

$$\alpha = \left(\frac{-(1-\omega)\Delta t}{c_{n,i,j,k}\Delta x} \right) \left(\frac{\lambda_{i-1/2,j,k}}{x_{i,j,k} - x_{i-1,j,k}} \right) \quad (25)$$

212

$$\beta = \left(\frac{-(1-\omega)\Delta t}{c_{n,i,j,k}\Delta y} \right) \left(\frac{\lambda_{i,j-1/2,k}}{y_{i,j,k} - y_{i-1,j,k}} \right) \quad (26)$$

213

$$\gamma = \left(\frac{-(1-\omega)\Delta t}{c_{n,i,j,k}\Delta z} \right) \left(\frac{\lambda_{i,j,k-1/2}}{z_{i,j,k} - z_{i,j,k-1}} \right) \quad (27)$$

214

$$\eta = \left(\frac{-(1-\omega)\Delta t}{c_{n,i,j,k}\Delta x} \right) \left(\frac{\lambda_{i+1/2,j,k}}{x_{i+1,j,k} - x_{i,j,k}} \right) \quad (28)$$

215

$$\mu = \left(\frac{-(1-\omega)\Delta t}{c_{n,i,j,k}\Delta y} \right) \left(\frac{\lambda_{i-1/2,j,k}}{y_{i+1,j,k} - y_{i,j,k}} \right) \quad (29)$$

216

$$\phi = \left(\frac{-(1-\omega)\Delta t}{c_{n,i,j,k}\Delta z} \right) \left(\frac{\lambda_{i-1/2,j,k}}{z_{i+1,j,k} - z_{i,j,k}} \right) \quad (30)$$

217

$$\begin{aligned}
\zeta = 1 + & \left(\frac{(1-\omega)\Delta t}{c_{n_{i,j,k}}\Delta x} \right) \left[\frac{\lambda_{i-1/2,j,k}}{x_{i,j,k} - x_{i-1,j,k}} + \frac{\lambda_{i+1/2,j,k}}{x_{i+1,j,k} - x_{i,j,k}} \right] \\
& + \left(\frac{(1-\omega)\Delta t}{c_{n_{i,j,k}}\Delta y} \right) \left[\frac{\lambda_{i,j-1/2,k}}{y_{i,j,k} - y_{i-1,j,k}} + \frac{\lambda_{i,j+1/2,k}}{y_{i+1,j,k} - y_{i,j,k}} \right] \\
& + \left(\frac{(1-\omega)\Delta t}{c_{n_{i,j,k}}\Delta z} \right) \left[\frac{\lambda_{i,j,k-1/2}}{z_{i,j,k} - z_{i,j,k-1}} + \frac{\lambda_{i,j,k+1/2}}{z_{i+1,j,k} - z_{i,j,k}} \right]
\end{aligned} \tag{31}$$

218

219 The column vector φ is given by

220

$$\begin{aligned}
\varphi = T_{i,j,k}^t + & \left(\frac{\omega\Delta t}{c_{n_{i,j,k}}\Delta x} \right) (F_{x_{i-1/2,j,k}}^t - F_{x_{i+1/2,j,k}}^t) \\
& + \left(\frac{\omega\Delta t}{c_{n_{i,j,k}}\Delta y} \right) (F_{y_{i,j-1/2,k}}^t - F_{y_{i,j+1/2,k}}^t) \\
& + \left(\frac{\omega\Delta t}{c_{n_{i,j,k}}\Delta z} \right) (F_{z_{i,j,k-1/2}}^t - F_{z_{i,j,k+1/2}}^t)
\end{aligned} \tag{32}$$

221

222 The coefficients of equation (24) described in equation (25)-(32) are for an internal grid
223 cell with six neighbors. The coefficients for the top grid cells are modified for presence of
224 snow and/or standing water. A no-flux boundary condition was applied on the bottom grid
225 cells, thus no geothermal flux was accounted for in this study. The coefficients for the grid
226 cells on the lateral boundary are modified for a no-flux boundary condition. ELM handles
227 ice-liquid phase transitions by first predicting temperatures at the end of a time step and
228 then updating temperatures after accounting for deficits or excesses of energy during
229 melting or freezing. See Oleson (2013b) for details about the computation of thermal
230 properties and phase transition.

231 2.3.3 PETSc Numerical solution

232 ELMv0, which considers flow only in the vertical direction, solves a tridiagonal and
233 banded tridiagonal system of equations for water and energy transport, respectively. In
234 ELM-3D, accounting for lateral flow in the subsurface results in a sparse linear system,
235 equations (10) and (24), where the sparcity pattern of the linear system depends on grid

236 cell connectivity. In this work, we use the PETSc (Portable, Extensible Toolkit for Scientific
237 Computing) library (Balay et al., 2016) developed at the Argonne National Laboratory to
238 solve the sparse linear systems. PETSc provides object-oriented data structures and solvers
239 for scalable scientific computation on parallel supercomputers. Description about the
240 numerical tests that were conducted to ensure the lateral coupling of hydrologic and
241 thermal processes was correctly implemented is presented in supplementary material
242 (Figure S 1 and S 2)

243 **2.4 Snow Model and Redistribution**

244 The snow model in ELM-3D is the same as that in the default ELMv0 and CLM4.5
245 (Anderson, 1976; Dai and Zeng, 1997; Jordan, 1991), except for the inclusion of snow
246 redistribution (SR). The snow model allows for a dynamic snow depth and up to five snow
247 layers, and explicitly solves the vertically-resolved mass and energy budgets. Snow aging,
248 compaction, and phase change are all represented in the snow model formulation.
249 Additionally, the snow model accounts for the influence of aerosols (including black and
250 organic carbon and mineral dust) on snow radiative transfer (Oleson, 2013a). ELMv0 uses
251 the methodology of Swenson and Lawrence (2012) to compute fractional snow cover area,
252 which is appropriate for ESM-scale grid cells (~100 km x 100 km). Since the grid cell
253 resolution in this work is sub-meter, we modified the fractional cover to be either 1 (when
254 snow was present) or 0 (when snow was absent).

255 Two main drivers of SR include topography and surface wind (Warscher et al.,
256 2013); previous SR models include mechanistically- (Bartelt and Lehning, 2002; Liston and
257 Elder, 2006) and empirically- (Frey and Holzmann, 2015; Helfricht et al., 2012) based
258 approaches. To mimic the effects of wind, we used a conceptual model to simulate SR over
259 the fine-resolution topography of our site by instantaneously re-distributing the incoming
260 snow flux such that lower elevation areas (polygon center) receive snow before higher
261 elevation areas (polygon rims). This relatively simple and parsimonious approach is
262 reasonable given the observed snow depth heterogeneity, as described below, and small
263 spatial extent of our domain.

264 **2.5 System Characterization**

265 Hydrologic and thermal properties differ by depth and landscape type. We used the
266 horizontal distribution of organic matter (OM) content from Wainwright et al. (2015) to
267 infer soil hydrologic and thermal properties following the default representations in ELM.
268 Vegetation cover was classified as arctic shrubs in polygon centers and arctic grasses in
269 polygon rims. The default representation of the plant wilting factor assigns a value of zero
270 for a given soil layer when its temperature falls below a threshold ($T_{\text{threshold}}$) of $-2\text{ }^{\circ}\text{C}$. This
271 default value leads to overly large predicted latent and sensible heat fluxes during winter,
272 compared to nearby eddy covariance measurements. We modified $T_{\text{threshold}}$ to be $0\text{ }^{\circ}\text{C}$ in this
273 study, resulting in improved predicted wintertime latent heat fluxes compared to the
274 default version of the model (Figure S3). Although biases compared to the observations
275 remain, particularly for sensible heat fluxes in the spring, the improvement is substantial
276 and, given the observational uncertainties, we believe sufficient to justify our use of the
277 model for investigations of the role of snow heterogeneity in this polygonal tundra system.

278 **2.6 Simulation Setup, Climate Forcing, and Analyses**

279 Because of computational constraints, we investigated the role of snow
280 redistribution and physics representation using a two-dimensional transect through site A
281 (Figure 1). The transect was 104 m long and 45 m deep and was discretized horizontally
282 with a grid spacing of 0.25 m and an exponentially varying layer thickness in the vertical
283 with 30 soil layers. The transect does not align with the sensor locations because our
284 objective was not to validate the model for a few grid cells, but to focus on relative
285 differences between predictions for rims and centers of a polygon field. No flow conditions
286 for mass and energy were imposed on the east, west, and bottom boundaries of the domain.
287 Temporal discretization of 30 min was used in the simulations. All simulations were
288 performed in the “satellite phenology” (SP) mode, i.e., Leaf Area Index (LAI) was prescribed
289 from MODIS observations.

290 Simulations were run for 10 years using long-term climate data gathered at the
291 Barrow, Alaska Observatory site (<https://www.esrl.noaa.gov/gmd/obop/brw/>) managed
292 by the Global Monitoring Division of NOAA’s Earth System Research Laboratory (Mefford et
293 al., 1996). The missing precipitation time series was gap-filled using daily precipitation at

294 the Barrow Regional Airport available from the Global Historical Climatology Network
295 (<http://www1.ncdc.noaa.gov/pub/data/ghcn/daily>). We tested the model by comparing
296 predictions to high-frequency observations of snow depth and vertically resolved soil
297 temperature for September 2012 – September 2013. Temperature observations were
298 taken at discrete locations in a polygon center and rim (Figure 1), and were combined to
299 analyze comparable landscape positions in the simulations (Figure 2).

300 After testing, the model was used to investigate the effects of snow redistribution
301 and 2D subsurface hydrologic and thermal physics by analyzing three scenarios: (1) no
302 snow redistribution and 1D physics; (2) snow redistribution and 1D physics; and (3) snow
303 redistribution and 2D physics. Between these scenarios, we compared vertically-resolved
304 soil temperature and liquid saturation, active layer depth, and mean and spatial variation of
305 latent and sensible heat fluxes across the 10 years of simulations. For each soil column, the
306 simulated soil temperature was interpolated vertically and the active layer depth was
307 estimated as the maximum depth that had above-freezing soil temperature.

308 **3 Results and Discussion**

309 **3.1 Snow depth**

310 In the absence of SR, predicted snow depth exactly follows the topography. With SR,
311 a much smaller dependence of winter-average snow depth on topography is predicted
312 (Figure 2). Further, for the winter average, there are very small differences in snow depth
313 between simulations with SR and 1D or 2D subsurface physics representations. Compared
314 to observations, considering SR led to: (1) a factor of ~ 2 improvement in snow depth bias
315 for the polygon center; (2) modest increase and decrease in average bias on the rims for
316 September through February and March through June, respectively; and (3) a dramatic
317 improvement in bias of the difference in snow depth between the polygon centers and rims
318 (Figure 3). There was no discernible difference in snow depth bias between the 1D and 2D
319 physics (Table 1), although the predicted subsurface temperature fields were different, as
320 shown below.

321 The temporal variation of the mean snow depth (**Figure 4a**) and its spatial standard
322 deviation (**Figure 4b**) also differed based on whether SR was considered, but was not

323 affected by considering 2D thermal or hydrologic physics. With SR, the snow depth
324 coefficient of variation (**Figure 4c**) was about 0.5 from December through the beginning of
325 the snowmelt period, indicating relatively large spatial heterogeneity. Simulated snow
326 depth for the three simulation scenarios are included in Supplementary Material (4)

327 **3.2 Soil Temperature and Active Layer Depth**

328 Broadly, ELM-3D accurately predicted the polygon center soil temperature at depth
329 intervals corresponding to the temperature probes (0-20 cm, 20-50 cm, 50-75 cm, and 75-
330 100 cm; Figure 5a). Recall that the observed temperatures for the polygon center and rims
331 were taken at single points in site A (Figure 1) while the predicted temperatures were
332 calculated as averages across the transect for each of the two landscape position types. The
333 model was able to simulate early freeze up of the soil column under the rims as compared
334 to centers in November 2012 because of differences in accumulated snow pack. The
335 transition to thawed soil in the 0-20 cm depth interval in early June 2013 and the
336 subsequent temperature dynamics over the summer were very well captured by ELM-3D.
337 Minimum temperatures during the winter were also accurately predicted, although the
338 temperatures in the deepest layer (75-100 cm) were overestimated by $\sim 3^{\circ}\text{C}$ in March. For
339 figure clarity we did not indicate the standard deviation of the observations, but provide
340 that information in Supplemental Material (Figure S5-S8).

341 Similarly, the soil temperatures were accurately predicted in the polygon rims
342 (Figure 5b). The largest discrepancies between measured and predicted soil temperatures
343 were in the shallowest layer (0 - 25 cm), where the predictions were up to a few $^{\circ}\text{C}$ cooler
344 than some of the observations between December 2012 and March 2013. In the polygon
345 center, a thicker snow pack acts as a heat insulator and keeps soil temperature higher in
346 winter as compared to the polygon rims.

347 Three recent studies have used other mechanistic models to simulate soil
348 temperature fields at this site, and achieved comparably good comparisons with
349 observations (Kumar et al. 2016 applied a 3D version of PFLOTRAN; Atchley et al. 2015 and
350 Harp et al. 2016 applied a 1D version of ATS). However, those models used measured soil
351 temperatures near the surface as the top boundary condition. In contrast, the top boundary
352 condition in this work is the climate forcing (air temperature, wind, solar radiation,

353 humidity, precipitation), and the ground heat flux is prognosed based on ELM's vegetation
354 and surface energy dynamics. We note that no parameter calibration was done in this work
355 or that of Kumar et al. (2016), while the ATS parameterizations were calibrated to match
356 the soil temperature profile.

357 Snow redistribution impacts spatial variability of soil temperature throughout the
358 soil column. Absence of SR results in no significant spatial variability of soil temperature
359 (Figure 6a). Inclusion of SR on the surface modifies the amount of energy exchanged
360 between the snow and the top soil layer, thereby creating spatial variability in the
361 temperature of the top soil, which propagates down into the soil column (Figure 6b). With
362 SR, energy dissipation in the lateral direction reduces the penetration depth of the soil
363 temperature spatial variance (compare Figure 6c and Figure 6b).

364 With 1D physics, the average spatial and temporal difference of the active layer
365 depth (ALD) between simulations with and without SR was 1.7 cm (Figure 7a), and the
366 absolute difference was 6.5 cm. As described above, we diagnosed the ALD to be the
367 maximum soil depth during the summer at which vertically interpolated soil temperature
368 is 0 °C. On average, the rims had ~10 cm shallower ALD with (blue line) than without
369 (green line) SR, consistent with the loss of insulation from SR on the rims during the
370 winter. In the centers (e.g., at location 42 - 55 m), the thaw depth was deeper by ~5 cm
371 with SR because of the higher snow depth there from SR. The effect of SR on the ALD was
372 largest on the rims because, compared to centers, they (1) on average lost more snow with
373 SR and (2) are more thermally conductive. Since rims are therefore colder at the time of
374 snowmelt with SR, the ground heat flux during the subsequent summer was unable to thaw
375 the soil column as deeply as when SR is ignored. For comparison, Atchley et al. (2015)
376 found in their sensitivity analysis using the 1D version of ATS that SR resulted in deeper
377 thaw depths in both polygon centers (by ~3 cm) and rims (~0.3 cm). Thus, their results for
378 polygon centers are consistent in sign but lower in magnitude than ours, but opposite in
379 sign for the rims.

380 Across ten years of simulation, the inter-annual variability (IAV) in ALD varied
381 substantially between the three scenarios (Figure 7b). As expected, for the 1D physics
382 without SR scenario (green line), the IAV in ALD was determined by landscape position
383 because of differences in soil and vegetation parameters. With SR and 1D physics, the

384 model shows largest differences over the rims, again highlighting the relatively larger
385 effects of SR on the rim soil temperatures.

386 The effect of 1D versus 2D physics on the ALD across the transect was modest
387 (mean absolute difference ~ 3 cm). Generally, because 2D physics allows for lateral energy
388 diffusion, the horizontal variation of ALD was slightly lower (i.e., the red line is smoother
389 than the blue line; Figure 7a) than with 1D physics. This difference was also reflected in the
390 thaw depth IAV across the transect, where 2D physics led to a smoother lateral profile of
391 inter-annual variability than with 1D physics.

392 The impact of physics formulation (i.e., 1D or 2D) alone was investigated by
393 analyzing differences between soil temperature profiles over time for polygon rims and
394 centers in simulations with snow redistribution. Inclusion of 2D subsurface physics
395 resulted in soil temperatures with depth and time that were lower in the polygon rims
396 (Figure 8a) and higher in polygon centers (Figure 8b). Using the simulations from the
397 scenario with SR and 2D physics, we evaluated the extent to which soils under rims and
398 centers can be separately considered as relatively homogeneous single column systems by
399 evaluating the soil temperature standard deviation as a function of depth and time (Figure
400 9). During winter, both polygon rims and centers were predicted to have soil temperature
401 spatial variability > 1 °C up to a depth of ~ 2 m. The soil temperature spatial variability in
402 winter due to snow redistribution was dissipated over the summer. During the summer,
403 polygon centers were relatively more homogeneous vertically compared to polygon rims.

404 **3.3 Surface Energy Budget**

405 Predicted monthly- and spatial-mean (μ) surface latent heat fluxes across the
406 transect were very similar between the three scenarios (Figure 10a), with a growing
407 seasonal mean difference of < 1.0 W m⁻². However, the spatial variability ($SV = \sigma$; Figure
408 10b) and coefficient of variation ($CV = \sigma/\mu$; Figure 10c) of latent heat fluxes were different
409 between the scenarios with SR (1D and 2D physics) and without SR. With SR, the latent
410 heat flux spatial standard deviation peaked after snowmelt and declined until the fall when
411 snow began, from about $\sim 100\%$ to 10% of the mean. This relatively larger spatial variation
412 in latent heat flux occurred because of large spatial heterogeneity in near surface soil

413 moisture in the beginning of summer, indicating a residual effect of SR from the previous
414 winter.

415 The predicted temporal monthly-mean and spatial-mean surface sensible heat
416 fluxes across the transect were also similar between the three scenarios (Figure 11a), with
417 a growing season mean absolute difference of $< 3.5 \text{ W m}^{-2}$. Also, the sensible heat flux
418 spatial variability differences occurred earlier than snowmelt, in contrast to the latent heat
419 flux. Both the standard deviation and CV of the sensible heat fluxes were larger than those
420 of the latent heat fluxes, with early season standard deviations of $\sim 50 \text{ W m}^{-2}$ (Figure 11b)
421 and CV's of ~ 1.5 (Figure 11c). As for the latent heat fluxes, the differences in standard
422 deviation and CV of sensible heat fluxes were small between the 1D and 2D scenarios with
423 SR, arguing that the subsurface lateral energy exchanges associated with the 2D physics did
424 not propagate to the mean surface heat fluxes. However, as for the latent heat flux, there
425 was a relatively large difference in spatial variation between the scenarios with and
426 without SR (e.g., of about 25 W m^{-2} in May; Figure 10b).

427 **3.4 Soil Moisture**

428 Neither SR nor 2D lateral physics affected the spatial mean moisture across time
429 (not shown). However, spatial heterogeneity of predicted soil moisture content differed
430 substantially between scenarios during the snow free period (Figure 12). For the 1D
431 simulations, the effect of SR was to increase growing season soil moisture spatial
432 heterogeneity by factors of 5.2 and 1.6 for 0-10 cm and 10-65 cm depth intervals,
433 respectively (compare Figure 12a and Figure 12b). Compared to 1D physics, simulating 2D
434 thermal and hydrologic physics led to an overall reduction in soil moisture spatial
435 heterogeneity by factors of 0.8 and 0.7 for 0-10 cm and 10-65 cm depth intervals,
436 respectively (compare Figure 12b and Figure 12c). Thus, with respect to dynamic spatial
437 mean soil moisture, SR effects dominated those associated with lateral subsurface water
438 movement.

439 **3.5 Caveats and Future Work**

440 The good agreement between ELM-3D predictions and soil temperature
441 observations demonstrate the model's capabilities to represent this very spatially

442 heterogeneous and complex system. However, several caveats to our conclusions remain
443 due to uncertainties in model parameterizations, model structure, and climate forcing data.

444 ELMv0, a one-dimensional model, is embarrassing parallel with no cross processor
445 communication. The current implementation of the three-dimensional solver in ELM-3D
446 only supports serial computing. Support of parallel computing will be included in a future
447 version of the model. Because of computational constraints, we applied a 2D transect
448 domain to the site, instead of a full 3D domain. We are working to improve the
449 computational efficiency of the model, which will facilitate a thorough analysis of the
450 effects of 3D subsurface energy and water fluxes. A related issue is our simplified treatment
451 of surface water flows. A thorough analysis of the effects of surface water redistribution
452 would require integration of a 2D surface thermal flow model in a 3D domain, which is
453 another goal for our future work. However, we note that the good agreement using the 2D
454 model domain supports the idea that a two-dimensional simplification may be appropriate
455 for this system. The expected geomorphological changes in these systems over the coming
456 decades (e.g., Liljedahl et al. 2016), which will certainly affect soil temperature and
457 moisture, are not currently represented in ELM, although incorporation of these processes
458 is a long-term development goal.

459 The current representation of vegetation in ELM-3D for these polygonal tundra
460 systems is over-simplified. For example, non-vascular plants (mosses and lichens) are not
461 explicitly represented in the model, but can be responsible for a majority of evaporative
462 losses (Miller et al., 1976) and are strongly influenced by near surface hydrologic
463 conditions (Williams and Flanagan, 1996). Our use of the 'satellite phenology' mode, which
464 imposes transient LAI profiles for each plant functional type in the domain, ignores the
465 likely influence of nutrient constraints (Zhu et al., 2016) on photosynthesis and therefore
466 the surface energy budget. Other model simplifications, e.g., the simplified treatment of
467 radiation competition may also be important, especially as simulations are extended over
468 periods where vegetation change may occur (e.g., Grant 2016).

469 Development of sub grid parameterizations to parsimoniously capture fine scale
470 processes will be pursued in the future. For example, a two-tile approach to represent
471 hydrologic and thermal processes in coupled polygon rims and centers with snow
472 redistribution should be evaluated. Inclusion of lateral subsurface processes has a greater

473 impact on predicted subgrid variability than on spatially averaged states. Thus, one
474 possible extension of the current model would be to explicitly include an equation for the
475 temporal evolution of sub grid variability using the approach of Montaldo and Albertson
476 (2003). The use of reduced-order models (e.g., Pau et al. (2014); Liu et al. (2016)) is an
477 alternate approach to estimate fine scale hydrologic and thermal states from a coarse
478 resolution representation. Additionally, lateral subsurface processes can be included in the
479 land surface model via a range of numerical discretization approaches of varying
480 complexity, e.g., adding lateral water and energy fluxes as source/sink terms in the existing
481 1D model, implementing an operator split approach to solve vertical and lateral processes
482 in a non-iterative approach, or solving a fully coupled 3D model. Tradeoffs between
483 approaches that represent lateral processes and computational costs need to be carefully
484 studied before developing quasi or fully three-dimensional land surface models. While the
485 present study focused on application and validation of ELM-3D at fine-scale, future work
486 will focus on regional scale applications using comprehensive datasets and the Distributed
487 Model Intercomparison Project Phase 2 modeling protocol (Smith et al., 2012). Although
488 we found no significant effect of topography and SR on the $100\text{ m} \times 100\text{ m}$ grid-averaged
489 exchanges with the atmosphere, future work needs to analyze intermediate scale (e.g., 100
490 $\text{m} - 10\text{ km}$) topographical variation and the potential effects on biogeochemical and plant
491 processes and surface exchanges.

492 **4 Summary and Conclusions**

493 In a polygonal tundra landscape, we analyzed effects of microtopographical surface
494 heterogeneity and lateral subsurface transport on soil temperature, soil moisture, and
495 surface energy exchanges. Starting from the climate-scale land model ELMv0, we
496 incorporated in ELM-3D numerical representations of subsurface water and energy lateral
497 transport that are solved using PETSc. A simple method for redistributing incoming snow
498 along the microtopographic transect was also integrated in the model.

499 Over the observational record, ELM-3D with snow redistribution and lateral heat
500 and hydrological fluxes accurately predicted snow depth and soil temperature vertical
501 profiles in the polygon rims and centers (overall bias, RMSE, and R^2 of 0.59°C , 1.82°C and

502 0.99, respectively). In the rims, the transition to thawed soil in spring, summer
503 temperature dynamics, and minimum temperatures during the winter were all accurately
504 predicted. In the centers, a $\sim 2^{\circ}\text{C}$ warm bias in April in the 75-100 cm soil layer was
505 predicted, although this bias disappeared during snowmelt.

506 The spatial heterogeneity of snow depth during the winter due to snow
507 redistribution generated surface soil temperature heterogeneity that propagated into the
508 soil over time. The temporal and spatial variation of snow depth was affected by snow
509 redistribution, but not by lateral thermal and hydrologic transport. Both snow
510 redistribution and lateral thermal fluxes affected spatial variability of soil temperatures.
511 Energy dissipation in the lateral direction reduced the depth to which soil temperature
512 variance penetrated. Snow redistribution led to ~ 10 cm shallower active layer depths
513 under the polygon rims because of the residual effect of reduced insulation during the
514 winter. In contrast, snow redistribution led to ~ 5 cm deeper maximum thaw depth under
515 the polygon centers. The effect of lateral energy fluxes on active layer depths was ~ 3 cm.
516 Compared to 1D physics, the 2D subsurface physics led to lower (higher) soil temperatures
517 with depth and time in the polygon rims (centers). The larger than 1°C wintertime spatial
518 temperature variability down to ~ 2 m depth in rims and centers indicates the uncertainty
519 associated with considering rims and centers as separate 1D columns. During the summer,
520 polygon center temperatures were relatively more vertically homogeneous than
521 temperatures in the rims.

522 The monthly- and spatial-mean predicted latent and sensible heat fluxes were
523 unaffected by snow redistribution and lateral heat and hydrological fluxes. However, snow
524 redistribution led to spatial heterogeneity in surface energy fluxes and soil moisture during
525 the summer. Excluding lateral subsurface hydrologic and thermal processes led to an over
526 prediction of spatial variability in soil moisture and soil temperature because subsurface
527 gradients were artificially prevented from laterally dissipating over time. Snow
528 redistribution effects on soil moisture heterogeneity were larger than those associated
529 with lateral thermal fluxes.

530 Overall, our analysis demonstrates the potential and value of explicitly representing
531 snow redistribution and lateral subsurface hydrologic and thermal dynamics in polygonal
532 ground systems and quantifies the effects of these processes on the resulting system states

533 and surface energy exchanges with the atmosphere. The integration of a 3D subsurface
534 model in the E3SM Land Model also allows for a wide range of analyses heretofore
535 impossible in an Earth System Model context.

536

537 **5 Code availability**

538 The ELM-3D v1.0 code and data used in study are publicly available at

539 <https://bitbucket.org/gbisht/lateral-subsurface-model> and

540 <https://bitbucket.org/gbisht/notes-for-gmd-2017-71>.

541

542 **6 Tables**

543 **Table 1. Bias, root mean square error (RMSE), and correlation (R^2) between modeled and**
 544 **observed snow depth at polygon center, rim and difference between center and rim for**
 545 **2013 for three cases: Snow redistribution (SR) off and 1D physics, SR on and 1D physics,**
 546 **and SR on and 2D physics.**

	SR=Off, Physics=1D			SR=On, Physics=1D			SR=On, Physics=2D		
	Center	Rim	Center- Rim	Center	Rim	Center- Rim	Center	Rim	Center- Rim
Bias	-0.08	0.02	-0.10	-0.04	-0.03	-0.02	-0.04	-0.03	-0.02
RMSE	0.12	0.04	0.12	0.08	0.04	0.05	0.08	0.04	0.05
R^2	0.86	0.92	0.03	0.78	0.85	0.73	0.79	0.85	0.73

547

548

549 **Table 2 Bias, root mean square error (RMSE) and correlation (R^2) between modeled and**
 550 **observed soil temperature at polygon center and rim at multiple soil depth for 2013 for**
 551 **three cases: Snow redistribution (SR) off and 1D physics, SR on and 1D physics, and SR on**
 552 **and 2D physics.**

Bias						
	SR=Off, Physics=1D		SR=On, Physics=2D		SR=On, Physics=2D	
Depth [m]	Center	Rim	Center	Rim	Center	Rim
0.00 - 0.20	0.86	-1.73	-0.19	1.00	0.52	0.71
0.20 - 0.50	0.68	-1.52	-0.46	0.98	0.35	0.62
0.50 - 0.75	0.53	-1.49	-0.64	0.94	0.21	0.53
0.75 - 1.00	0.49	-1.44	-0.67	-0.97	0.22	0.49
Average across four depths	0.64	-1.54	-0.49	0.97	0.33	0.59

553

RMSE						
	SR=Off, Physics=1D		SR=On, Physics=2D		SR=On, Physics=2D	
Depth [m]	Center	Rim	Center	Rim	Center	Rim
0.00 - 0.20	2.11	3.39	2.20	2.94	1.90	2.66
0.20 - 0.50	1.49	2.73	1.39	1.86	1.12	1.57
0.50 - 0.75	1.60	2.42	1.22	1.96	1.14	1.60
0.75 - 1.00	1.50	2.15	1.12	1.87	1.09	1.44
Average across four depths	1.67	2.67	1.44	2.16	1.31	1.82

554

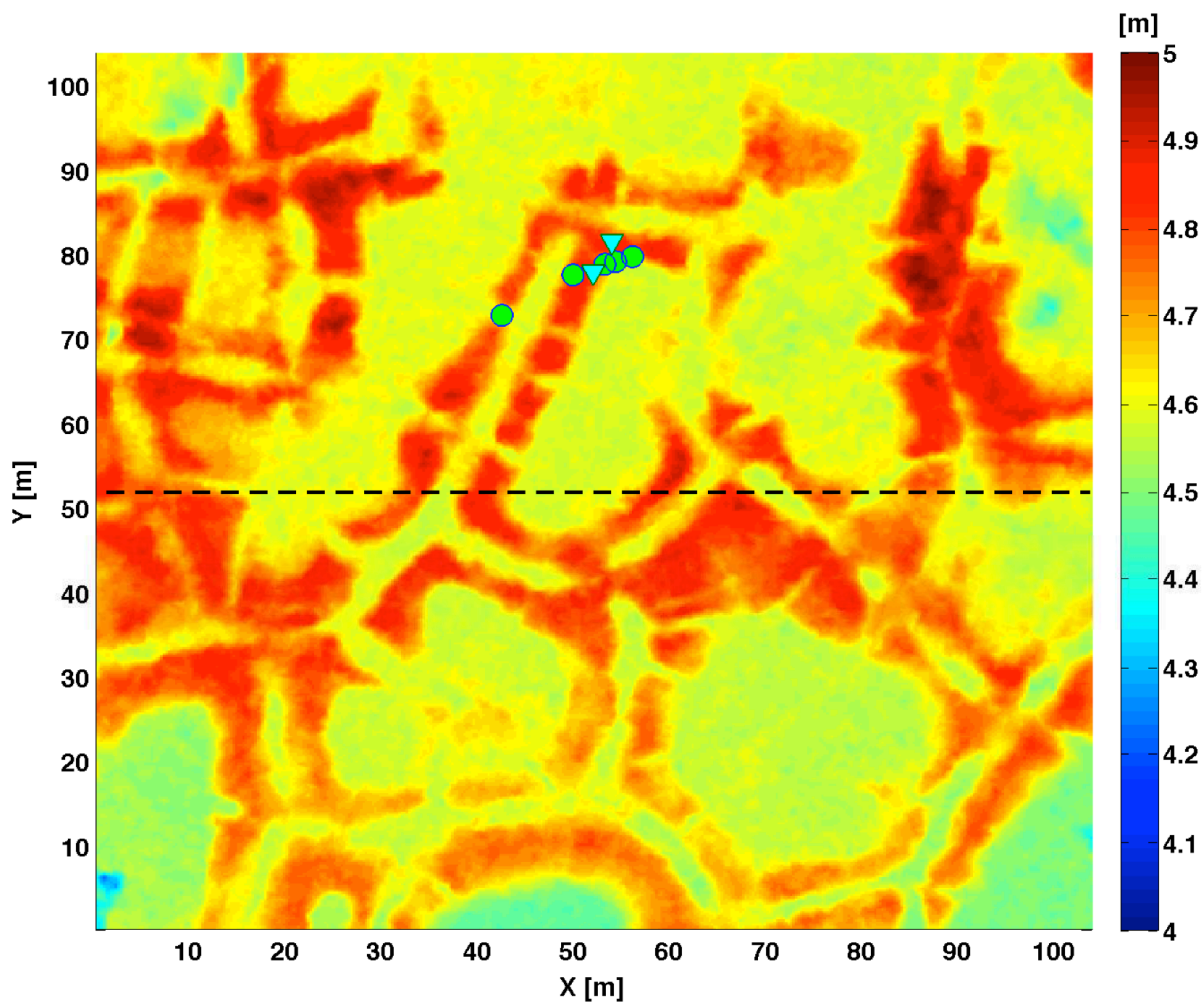
R^2						
	SR=Off, Physics=1D		SR=On, Physics=2D		SR=On, Physics=2D	
Depth [m]	Center	Rim	Center	Rim	Center	Rim
0.00 - 0.20	0.98	0.95	0.97	0.97	0.98	0.97

0.20 - 0.50	0.99	0.96	0.98	0.99	0.99	0.99
0.50 - 0.75	0.99	0.97	0.99	0.99	1.00	0.99
0.75 - 1.00	0.99	0.97	0.99	0.99	1.00	0.99
Average across four depths	0.99	0.96	0.98	0.99	0.99	0.99

555

556

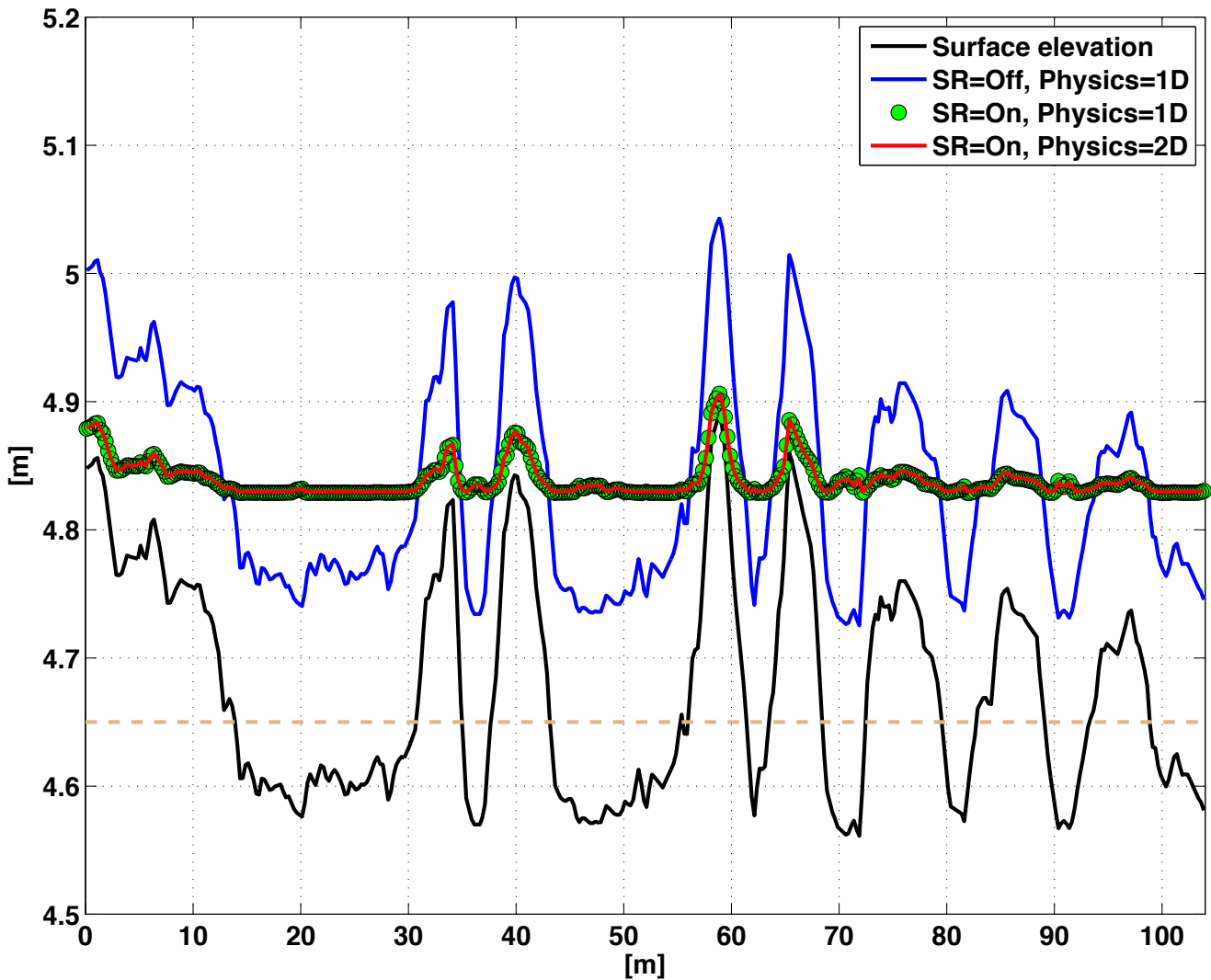
557 **7 Figures**



558

559 **Figure 1 The NGEE-Arctic study area A, which characterized as a low-centered polygon**
560 **field. Dotted line indicate the transect along which simulation in this paper are preformed**
561 **to demonstrate the effects of snow redistribution on soil temperature. The locations where**
562 **snow and temperature sensors are installed within the study site are denoted by triangle**
563 **and circle, respectively.**

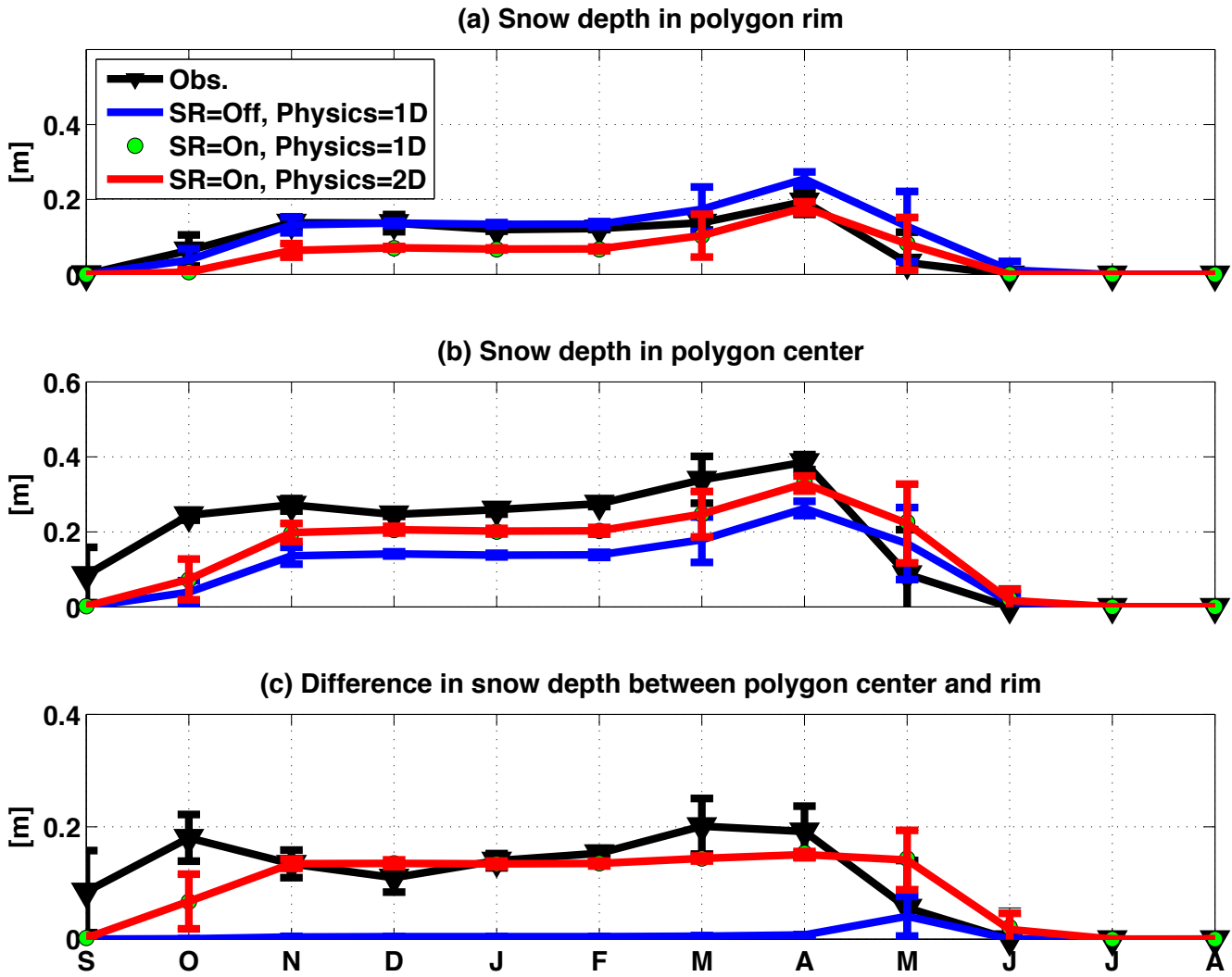
564



565

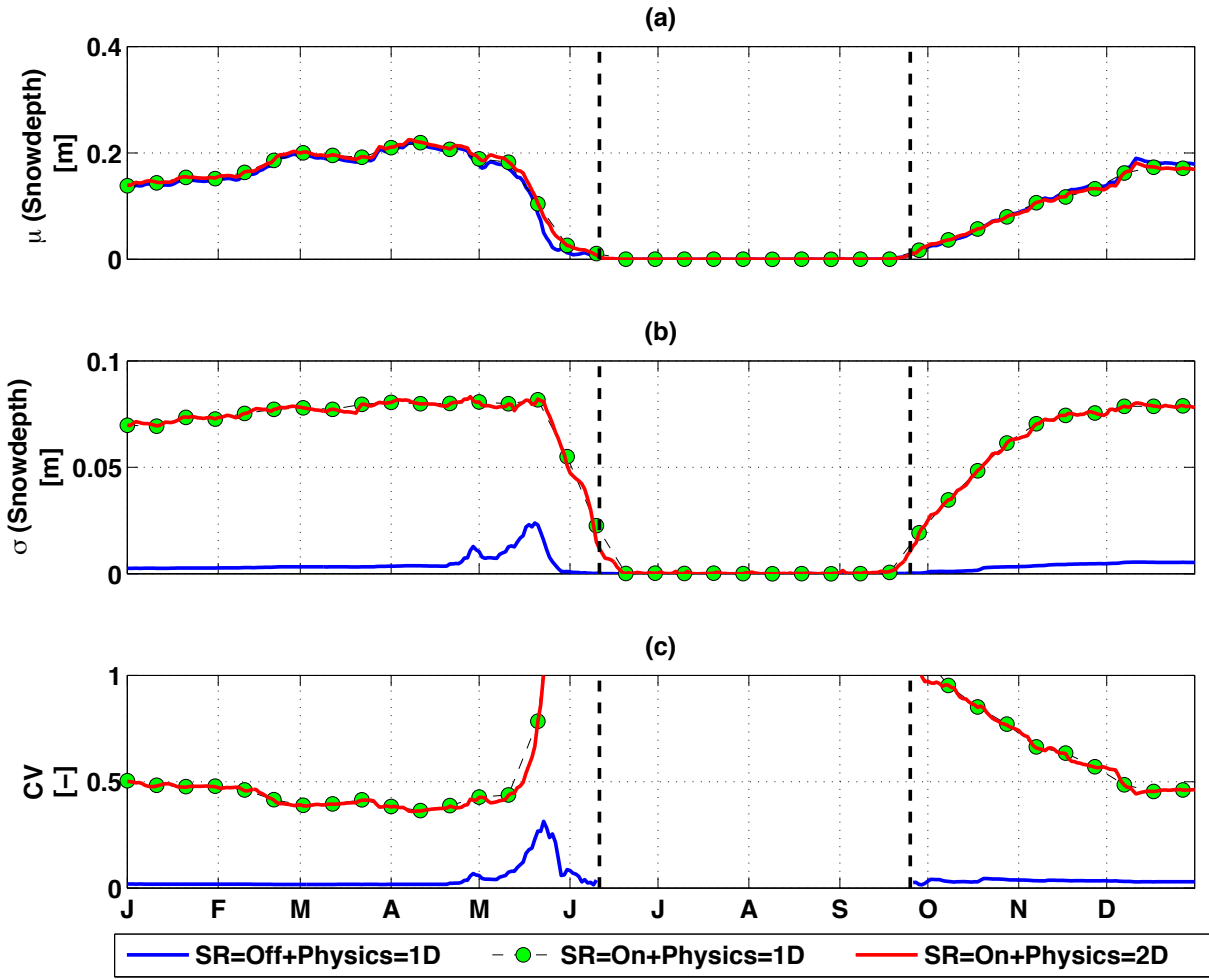
566 **Figure 2. Simulated average winter snow surface elevation across the transect for three**
 567 **scenarios: (1) snow redistribution (SR) turned off and 1D subsurface physics, (2) snow**
 568 **redistribution turned on and 1D subsurface physics, and (3) snow redistribution turned on**
 569 **and 2D subsurface physics. Surface elevation of the transect is shown by solid black line.**
 570 **The dashed line indicates the boundary for comparison to observations in relatively lower**
 571 **(centers) and relatively higher (rims) topographical positions.**

572
573



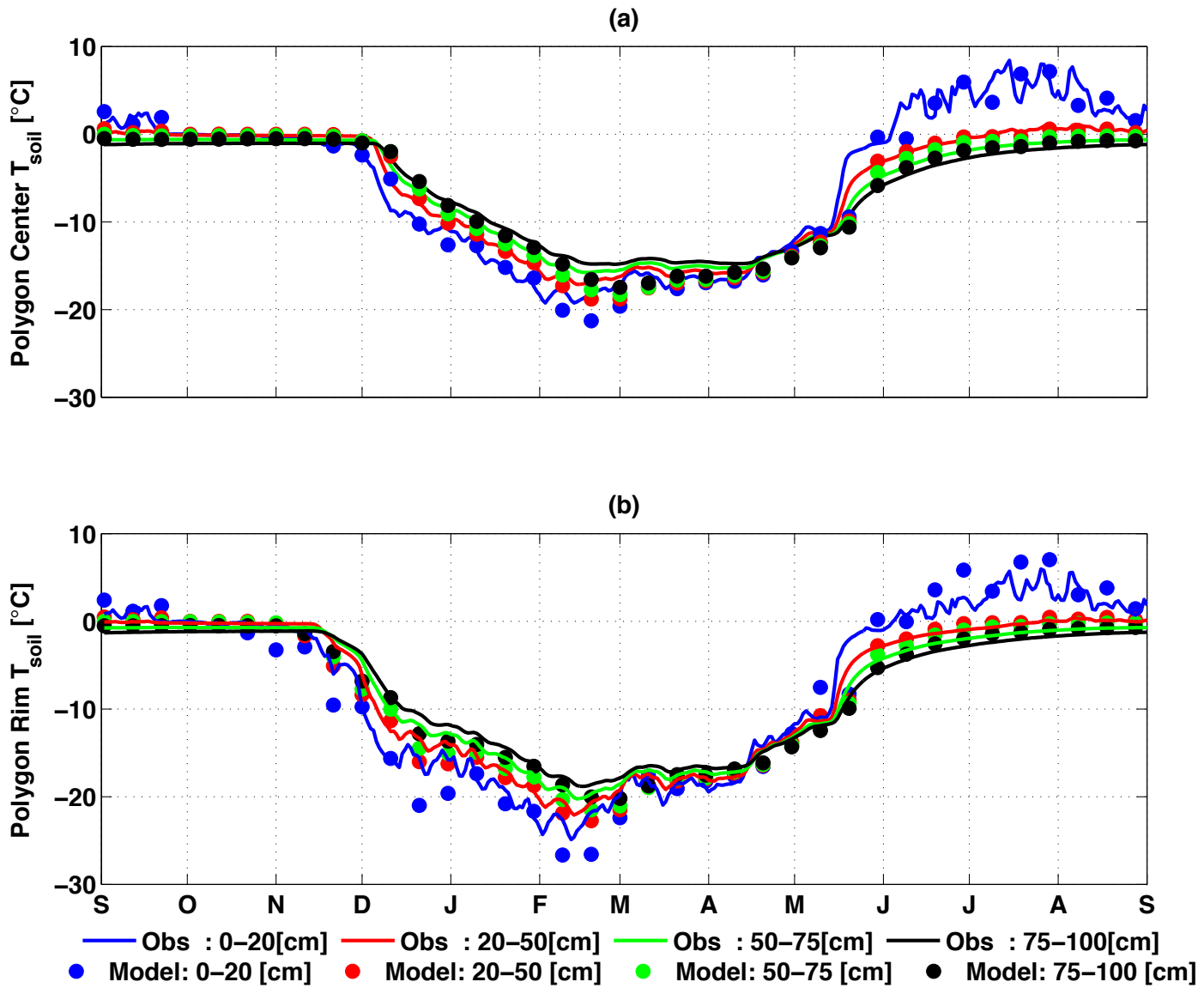
574
575
576
577

Figure 3 Monthly-mean comparison of observation and simulated snow depth (a) in polygon rim, (b) in polygon center; (c) difference between polygon center and rim for 2013.



578

579 **Figure 4. (a) Mean, (b) standard deviation and (c) coefficient of variation of**
 580 **simulated snow depth across the entire domain for 1D and 2D subsurface physics.**

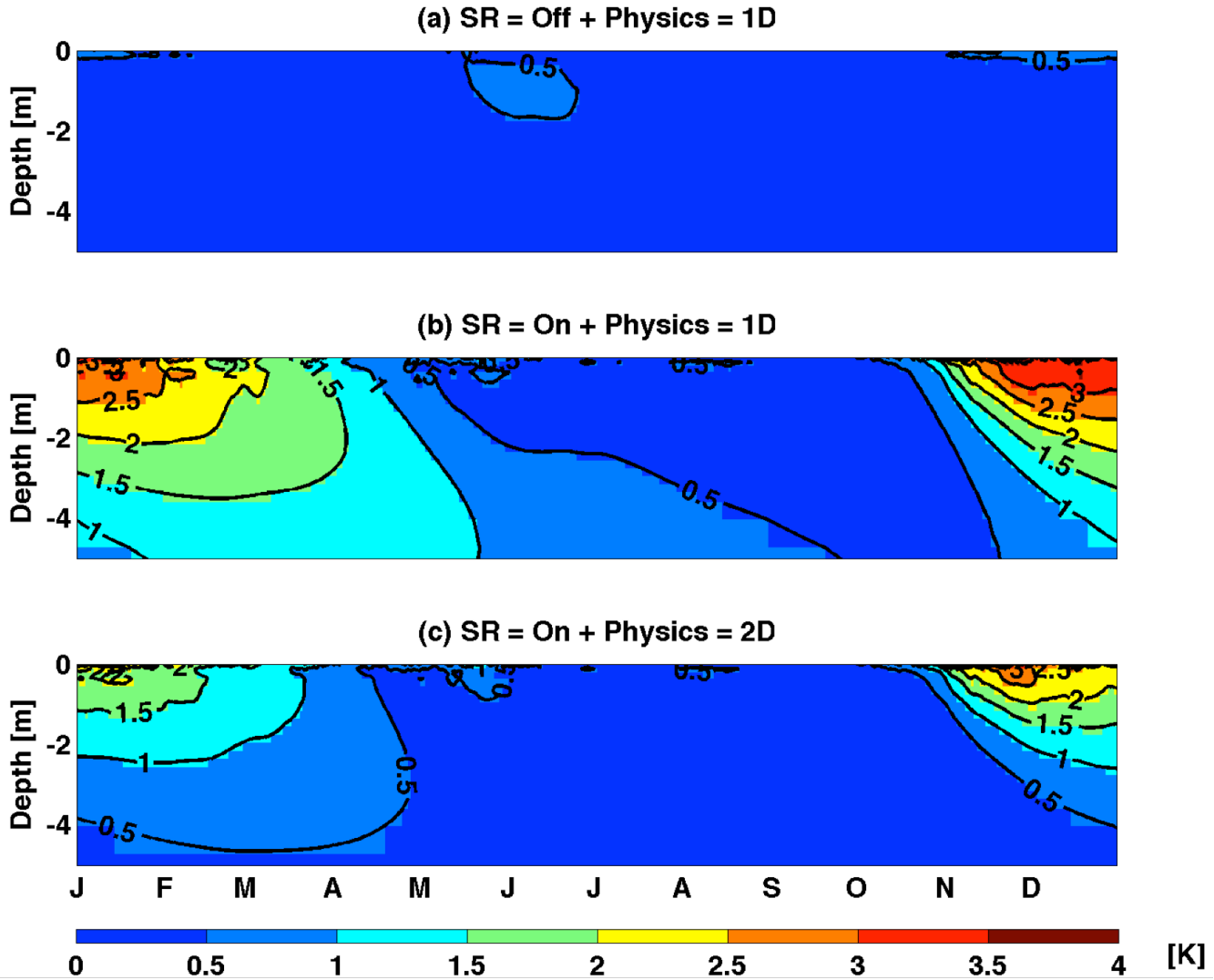


581

582 **Figure 5 Comparison of soil temperature observations and predictions in polygon centers**
 583 **(a) and rims (b). Simulation was performed with snow redistribution on and 2D subsurface**
 584 **physics, between September 2012 and September 2013. Simulation results are shown at an**
 585 **interval of 10 days, while observations are shown at daily interval**

586

587

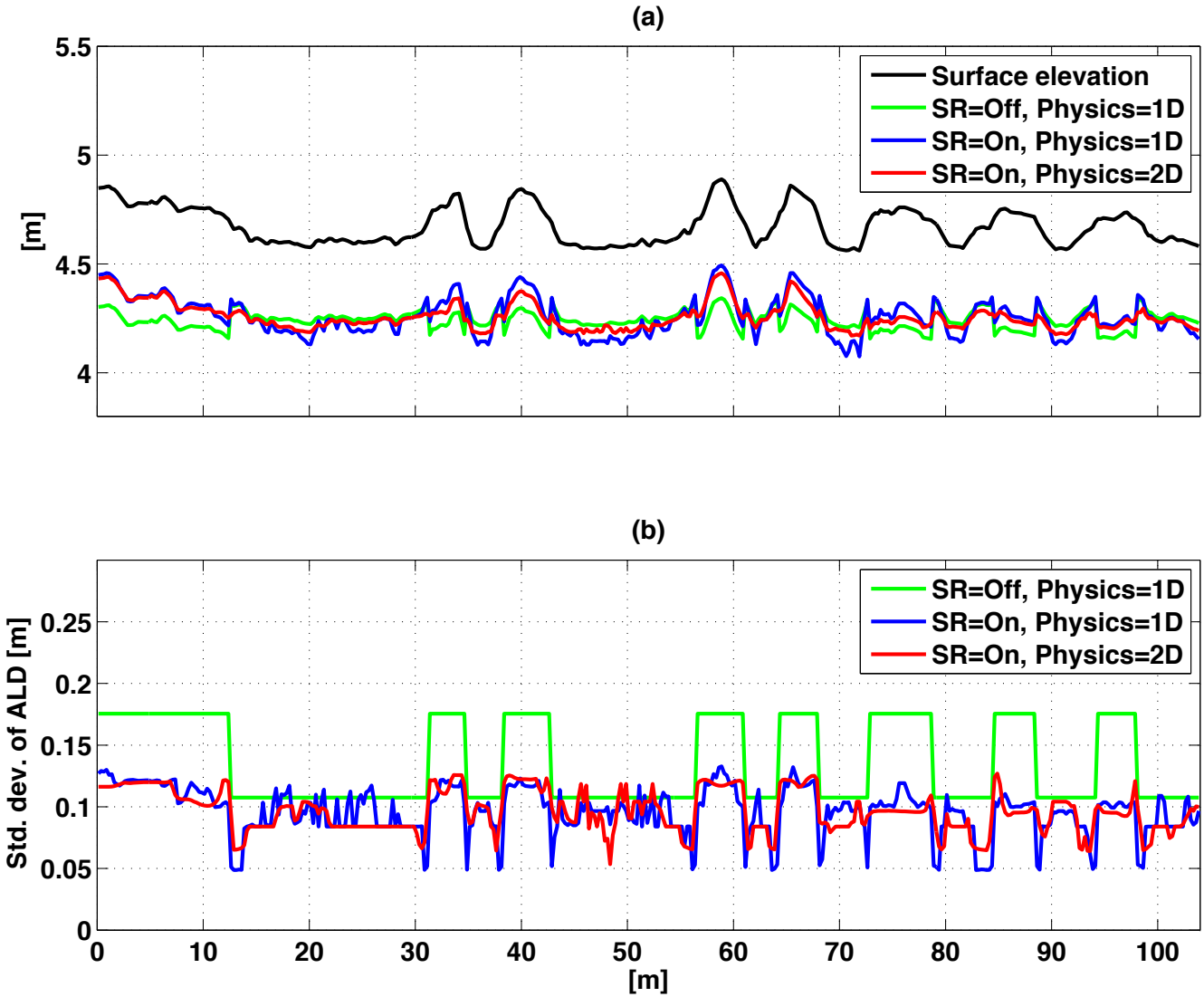


588

589 **Figure 6 Simulated daily spatial standard deviation for each soil layer averaged across 10-**
 590 **year of near surface soil temperature for simulation performed with snow redistribution**
 591 **turned off and 1D subsurface physics (top panel); snow redistribution turned on and 1D**
 592 **subsurface physics (middle panel); and snow redistribution turned on and 2D subsurface**
 593 **physics (bottom panel).**

594

595



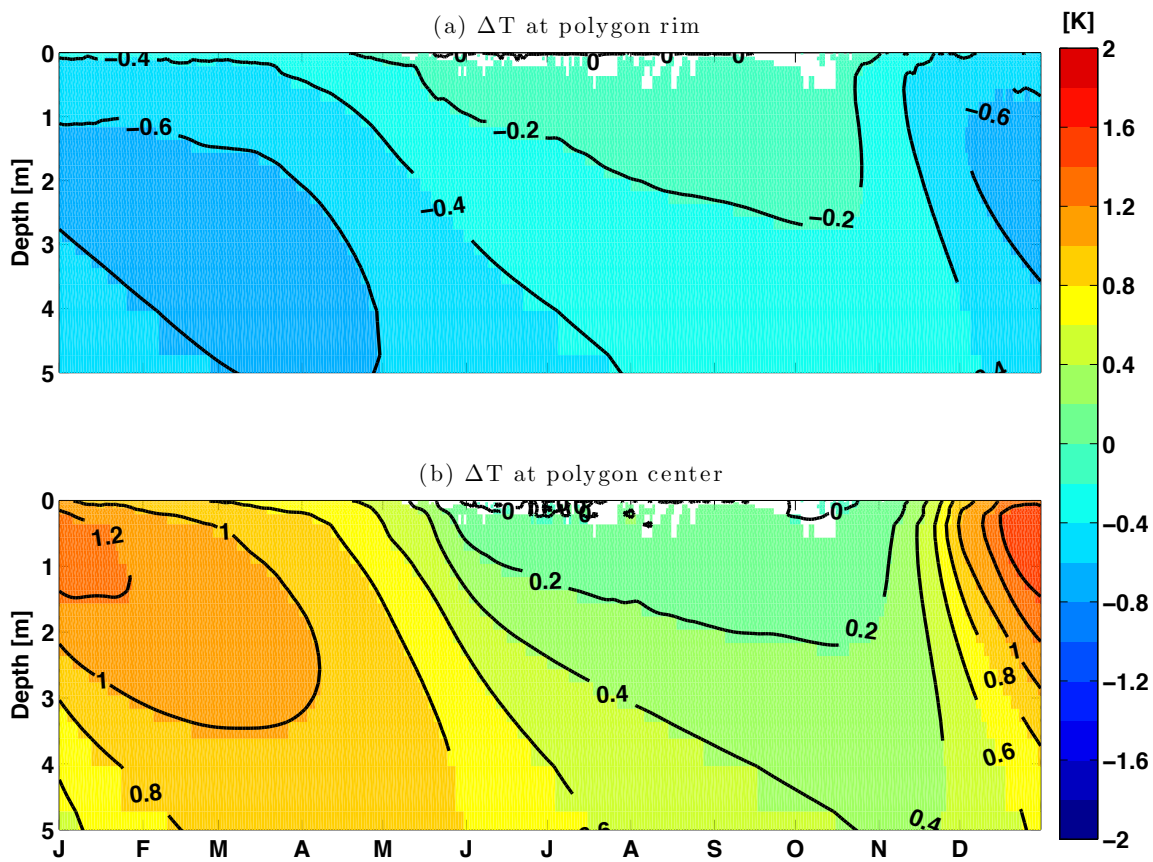
596

597

598 **Figure 7** Temporal mean of the bottom of the active layer (top panel) and standard
 599 deviation of the active layer depth (bottom panel) over the 10-year period across the
 600 modeling domain.

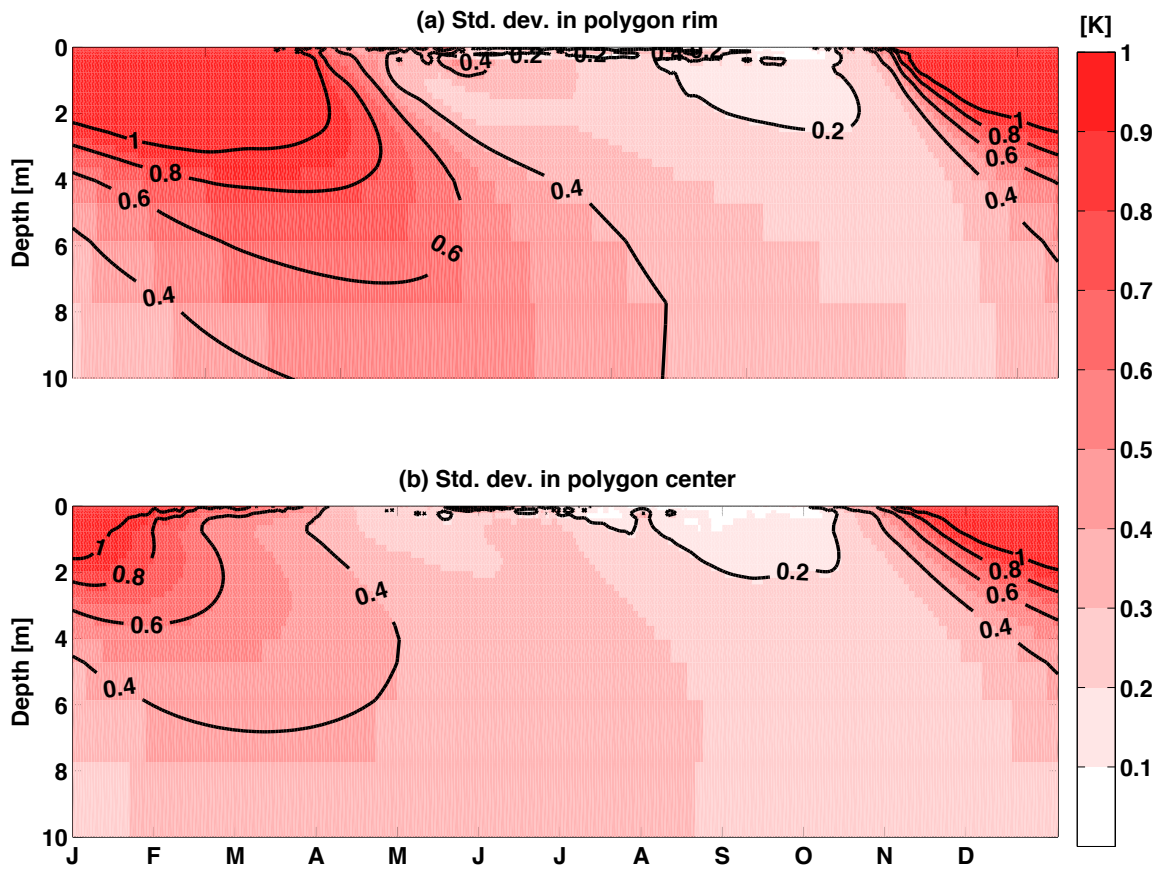
601

502
503



504

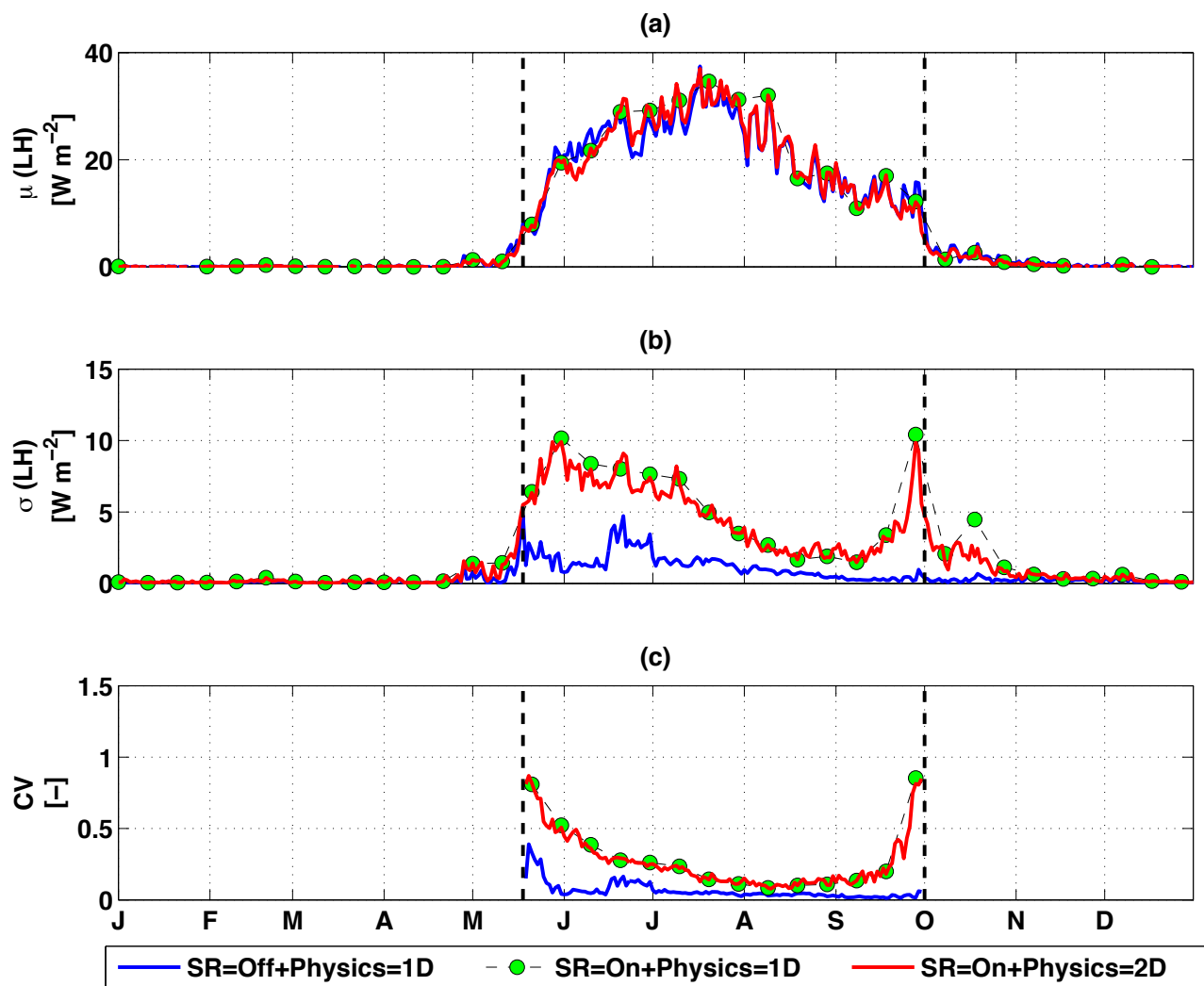
505 **Figure 8 Time series of spatial mean soil temperature differences between “SR=On +**
506 **Physics=1D” and “SR=On + Physics=2D” at polygon rim (top panel) and polygon center**
507 **(bottom panel).**



508

509 **Figure 9 Time series of soil temperature spatial standard deviation for “SR=On +**

510 **Physics=2D” at polygon rim (top panel) and polygon center (bottom panel).**



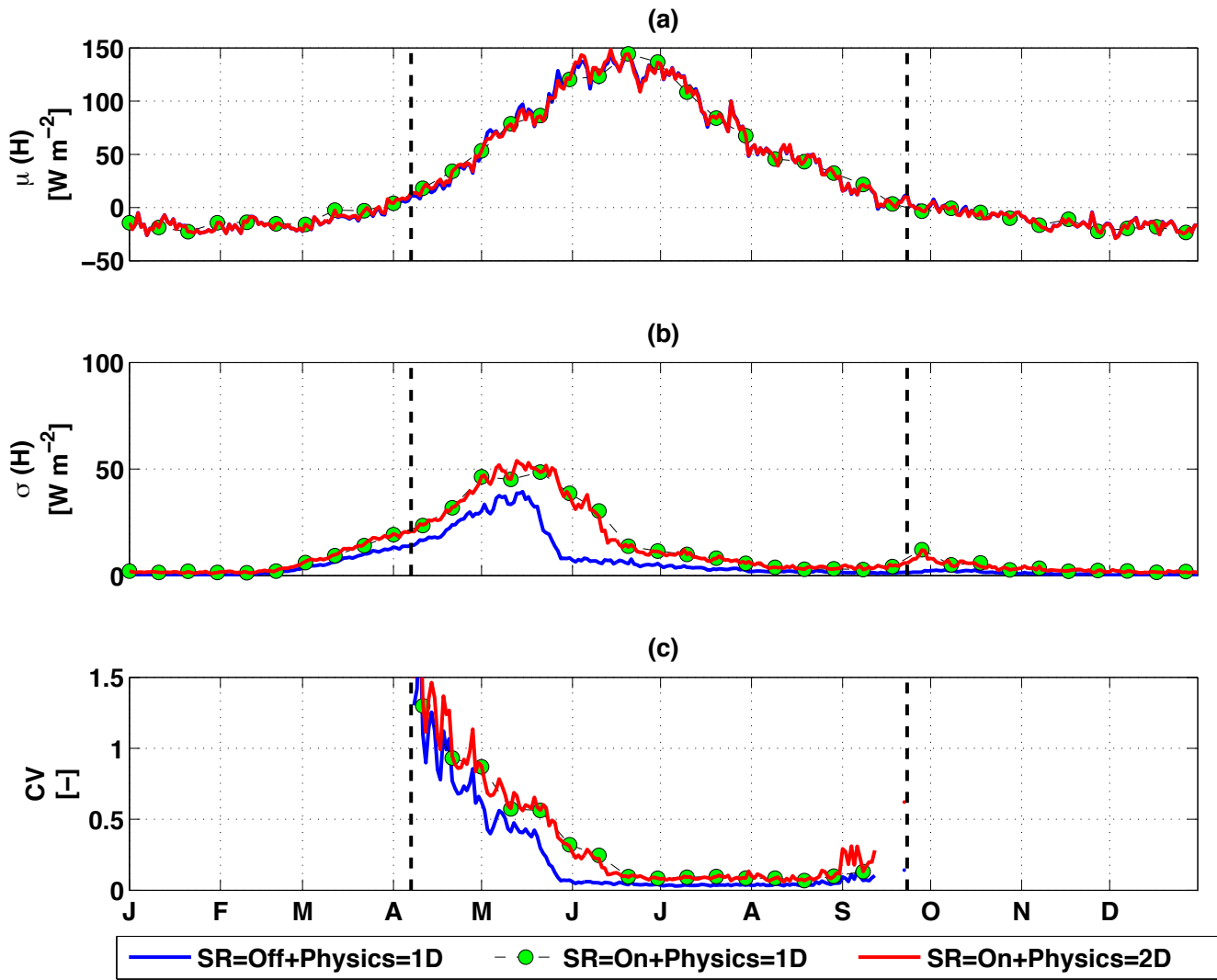
511

512

513 **Figure 10. Latent heat flux inter-annual (a) mean, (b) standard deviation, and (c)**

514 **coefficient of variation across the site A transect.**

515

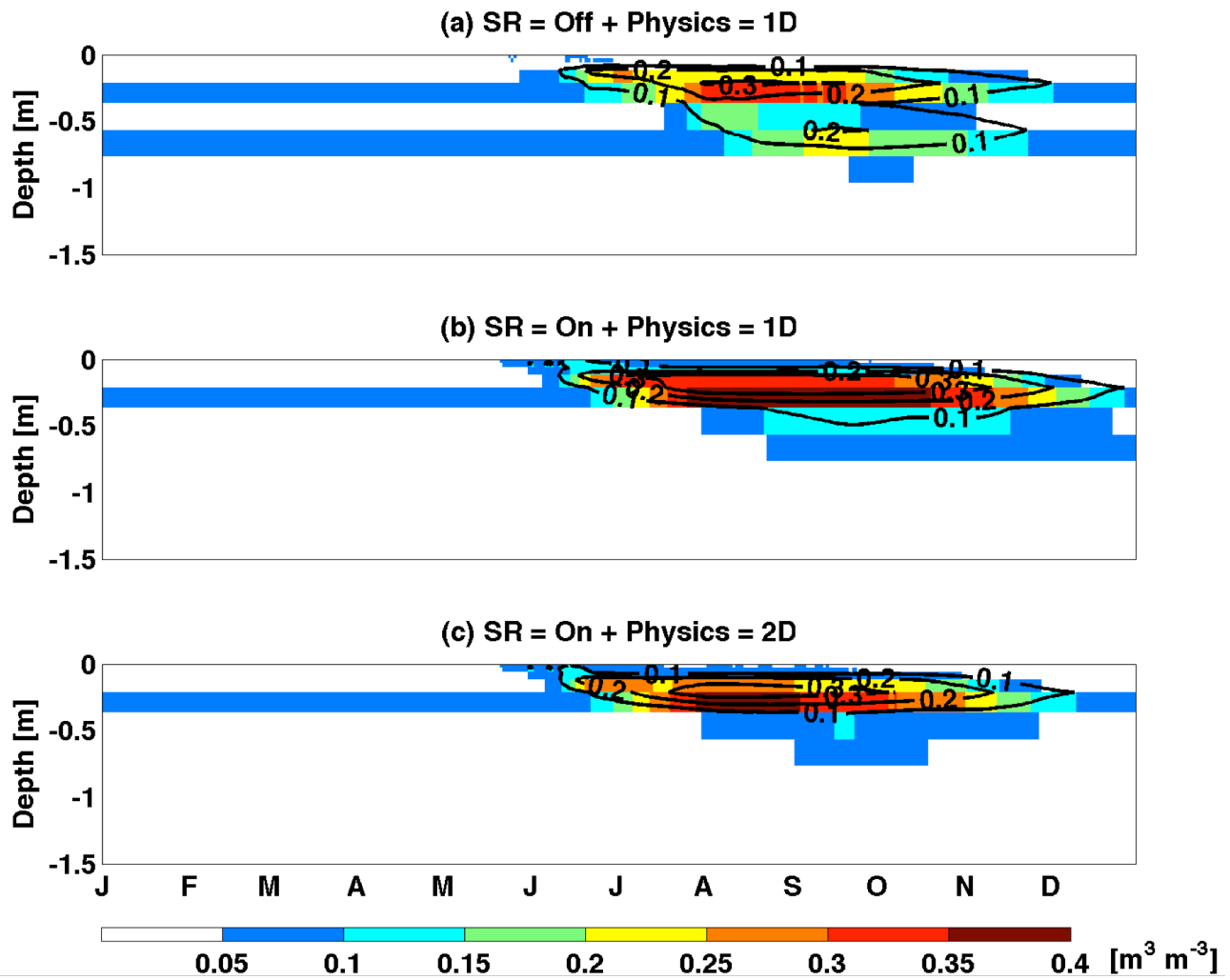


516

517

518 **Figure 11. Same as Figure 10 except for sensible heat flux.**

519



520

521 Figure 12. Same as Figure 6 except for liquid saturation.

522 **Acknowledgements.**

523 This research was supported by the Director, Office of Science, Office of Biological and
524 Environmental Research of the US Department of Energy under Contract No. DE-AC02-
525 05CH11231 as part of the NGEE-Arctic and Energy Exascale Earth System Model (E3SM)
526 programs.

527 **References**

- 528 Anderson, E. A.: A point energy and mass balance model of a snow cover, National Weather
529 Service, Silver Spring, MD, 1976.
- 530 Balay, S., Abhyankar, S., Adams, M. F., Brown, J., Brune, P., Buschelman, K., Dalcin, L.,
531 Eijkhout, V., Gropp, W. D., Kaushik, D., Knepley, M. G., McInnes, L. C., Rupp, K., Smith, B.
532 F., Zampini, S., Zhang, H., and Zhang, H.: PETSc Users Manual, Argonne National Laboratory,
533 2016.
- 534 Bartelt, P. and Lehning, M.: A physical SNOWPACK model for the Swiss avalanche warning:
535 Part I: numerical model, *Cold Regions Science and Technology*, 35, 123-145, 2002.
- 536 Borner, A. P., Kielland, K., and Walker, M. D.: Effects of Simulated Climate Change on Plant
537 Phenology and Nitrogen Mineralization in Alaskan Arctic Tundra, *Arctic, Antarctic, and Alpine*
538 *Research*, 40, 27-38, 2008.
- 539 Callaghan, T., Johansson, M., Brown, R., Groisman, P., Labba, N., Radionov, V., Barry, R.,
540 Bulygina, O., Essery, R. H., Frolov, D. M., Golubev, V., Grenfell, T., Petrushina, M., Razuvaev,
541 V., Robinson, D., Romanov, P., Shindell, D., Shmakin, A., Sokratov, S., Warren, S., and Yang,
542 D.: The Changing Face of Arctic Snow Cover: A Synthesis of Observed and Projected Changes,
543 *AMBIO*, 40, 17-31, 2011a.
- 544 Callaghan, T., Johansson, M., Brown, R., Groisman, P., Labba, N., Radionov, V., Bradley, R.,
545 Blangy, S., Bulygina, O., Christensen, T., Colman, J., Essery, R. H., Forbes, B., Forchhammer,
546 M., Golubev, V., Honrath, R., Juday, G., Meshcherskaya, A., Phoenix, G., Pomeroy, J., Rautio,
547 A., Robinson, D., Schmidt, N., Serreze, M., Shevchenko, V., Shiklomanov, A., Shmakin, A.,
548 Sköld, P., Sturm, M., Woo, M.-k., and Wood, E.: Multiple Effects of Changes in Arctic Snow
549 Cover, *AMBIO*, 40, 32-45, 2011b.
- 550 Clark, M. P., Hendrikx, J., Slater, A. G., Kavetski, D., Anderson, B., Cullen, N. J., Kerr, T., Örn
551 Hreinnsson, E., and Woods, R. A.: Representing spatial variability of snow water equivalent in
552 hydrologic and land-surface models: A review, *Water Resources Research*, 47, W07539, 2011.
- 553 Cox, P. M., Betts, R. A., Jones, C. D., Spall, S. A., and Totterdell, I. J.: Acceleration of global
554 warming due to carbon-cycle feedbacks in a coupled climate model, *Nature*, 408, 184-187, 2000.
- 555 Dai, Y. and Zeng, Q.: A land surface model (IAP94) for climate studies part I: Formulation and
556 validation in off-line experiments, *Advances in Atmospheric Sciences*, 14, 433-460, 1997.

557 Dufresne, J. L., Fairhead, L., Le Treut, H., Berthelot, M., Bopp, L., Ciais, P., Friedlingstein, P.,
558 and Monfray, P.: On the magnitude of positive feedback between future climate change and the
559 carbon cycle, *Geophysical Research Letters*, 29, 43-41-43-44, 2002.

560 Engstrom, R., Hope, A., Kwon, H., Stow, D., and Zamolodchikov, D.: Spatial distribution of
561 near surface soil moisture and its relationship to microtopography in the Alaskan Arctic coastal
562 plain, *Nordic Hydrology*, 36, 219-234, 2005.

563 Euskirchen, E. S., McGuire, A. D., Chapin, F. S., Yi, S., and Thompson, C. C.: Changes in
564 vegetation in northern Alaska under scenarios of climate change, 2003–2100: implications for
565 climate feedbacks, *Ecological Applications*, 19, 1022-1043, 2009.

566 Frey, S. and Holzmann, H.: A conceptual, distributed snow redistribution model, *Hydrol. Earth
567 Syst. Sci.*, 19, 4517-4530, 2015.

568 Friedlingstein, P., Bopp, L., Ciais, P., Dufresne, J.-L., Fairhead, L., LeTreut, H., Monfray, P.,
569 and Orr, J.: Positive feedback between future climate change and the carbon cycle, *Geophysical
570 Research Letters*, 28, 1543-1546, 2001.

571 Friedlingstein, P., Cox, P., Betts, R., Bopp, L., von Bloh, W., Brovkin, V., Cadule, P., Doney, S.,
572 Eby, M., Fung, I., Bala, G., John, J., Jones, C., Joos, F., Kato, T., Kawamiya, M., Knorr, W.,
573 Lindsay, K., Matthews, H. D., Raddatz, T., Rayner, P., Reick, C., Roeckner, E., Schnitzler, K.
574 G., Schnur, R., Strassmann, K., Weaver, A. J., Yoshikawa, C., and Zeng, N.: Climate–Carbon
575 Cycle Feedback Analysis: Results from the C4MIP Model Intercomparison, *Journal of Climate*,
576 19, 3337-3353, 2006.

577 Fung, I. Y., Doney, S. C., Lindsay, K., and John, J.: Evolution of carbon sinks in a changing
578 climate, *Proceedings of the National Academy of Sciences of the United States of America*, 102,
579 11201-11206, 2005.

580 Galen, C. and Stanton, M. L.: Responses of Snowbed Plant Species to Changes in Growing-
581 Season Length, *Ecology*, 76, 1546-1557, 1995.

582 Ghimire, B., Riley, W. J., Koven, C. D., Mu, M., and Randerson, J. T.: Representing leaf and
583 root physiological traits in CLM improves global carbon and nitrogen cycling predictions,
584 *Journal of Advances in Modeling Earth Systems*, 8, 598-613, 2016.

585 Govindasamy, B., Thompson, S., Mirin, A., Wickett, M., Caldeira, K., and Delire, C.: Increase
586 of carbon cycle feedback with climate sensitivity: results from a coupled climate and carbon
587 cycle model, *Tellus B*, 57, 2011.

588 Groendahl, L., Friberg, T., and Soegaard, H.: Temperature and snow-melt controls on
589 interannual variability in carbon exchange in the high Arctic, *Theoretical and Applied*
590 *Climatology*, 88, 111-125, 2007.

591 Grogan, P. and Chapin Iii, F. S.: Arctic Soil Respiration: Effects of Climate and Vegetation
592 Depend on Season, *Ecosystems*, 2, 451-459, 1999.

593 Hartman, M. D., Baron, J. S., Lammers, R. B., Cline, D. W., Band, L. E., Liston, G. E., and
594 Tague, C.: Simulations of snow distribution and hydrology in a mountain basin, *Water Resources*
595 *Research*, 35, 1587-1603, 1999.

596 Helfricht, K., Schöber, J., Seiser, B., Fischer, A., Stötter, J., and Kuhn, M.: Snow accumulation
597 of a high alpine catchment derived from LiDAR measurements, *Adv. Geosci.*, 32, 31-39, 2012.

598 Hinkel, K. M., Eisner, W. R., Bockheim, J. G., Nelson, F. E., Peterson, K. M., and Dai, X.:
599 Spatial Extent, Age, and Carbon Stocks in Drained Thaw Lake Basins on the Barrow Peninsula,
700 *Alaska, Arctic, Antarctic and Alpine Research*, 35, 291-300, 2003.

701 Hinkel, K. M., Frohn, R. C., Nelson, F. E., Eisner, W. R., and Beck, R. A.: Morphometric and
702 spatial analysis of thaw lakes and drained thaw lake basins in the western Arctic Coastal Plain,
703 *Alaska, Permafrost and Periglacial Processes*, 16, 327-341, 2005.

704 Hinzman, L. D. and Kane, D. L.: Potential repsonse of an Arctic watershed during a period of
705 global warming, *Journal of Geophysical Research: Atmospheres*, 97, 2811-2820, 1992.

706 Holland, M. M. and Bitz, C. M.: Polar amplification of climate change in coupled models,
707 *Climate Dynamics*, 21, 221-232, 2003.

708 Jiang, D., Zhang, Y., and Lang, X.: Vegetation feedback under future global warming,
709 *Theoretical and Applied Climatology*, 106, 211-227, 2011.

710 Jones, C. D., Cox, P. M., Essery, R. L. H., Roberts, D. L., and Woodage, M. J.: Strong carbon
711 cycle feedbacks in a climate model with interactive CO₂ and sulphate aerosols, *Geophysical*
712 *Research Letters*, 30, 1479, 2003.

713 Jones, H. G.: The ecology of snow-covered systems: a brief overview of nutrient cycling and life
714 in the cold, *Hydrological Processes*, 13, 2135-2147, 1999.

715 Jordan, R. E.: One-dimensional temperature model for a snow cover : technical documentation
716 for SNTHERM.89, Cold Regions Research and Engineering Laboratory (U.S.) Engineer
717 Research and Development Center (U.S.), 1991.

718 Jorgenson, M. T., Shur, Y. L., and Pullman, E. R.: Abrupt increase in permafrost degradation in
719 Arctic Alaska, *Geophysical Research Letters*, 33, L02503, 2006.

720 Koven, C. D., Lawrence, D. M., and Riley, W. J.: Permafrost carbon–climate feedback is
721 sensitive to deep soil carbon decomposability but not deep soil nitrogen dynamics, *Proceedings*
722 *of the National Academy of Sciences*, 112, 3752-3757, 2015.

723 Koven, C. D., Riley, W. J., Subin, Z. M., Tang, J. Y., Torn, M. S., Collins, W. D., Bonan, G. B.,
724 Lawrence, D. M., and Swenson, S. C.: The effect of vertically resolved soil biogeochemistry and
725 alternate soil C and N models on C dynamics of CLM4, *Biogeosciences*, 10, 7109-7131, 2013.

726 Koven, C. D., Ringeval, B., Friedlingstein, P., Ciais, P., Cadule, P., Khvorostyanov, D., Krinner,
727 G., and Tarnocai, C.: Permafrost carbon-climate feedbacks accelerate global warming,
728 *Proceedings of the National Academy of Sciences*, 108, 14769-14774, 2011.

729 Lawrence, D. M. and Swenson, S. C.: Permafrost response to increasing Arctic shrub abundance
730 depends on the relative influence of shrubs on local soil cooling versus large-scale climate
731 warming, *Environmental Research Letters*, 6, 045504, 2011.

732 Liston, G. E. and Elder, K.: A Distributed Snow-Evolution Modeling System (SnowModel),
733 *Journal of Hydrometeorology*, 7, 1259-1276, 2006.

734 Liston, G. E., Haehnel, R. B., Sturm, M., Hiemstra, C. A., Berezovskaya, S., and Tabler, R. D.:
735 Instruments and Methods
736 <http://pub2web.metastore.ingenta.com/ns/>
737 Simulating complex snow distributions in windy environments using SnowTran-3D, *Journal of*
738 *Glaciology*, 53, 241-256, 2007.

739 Lopez-Moreno, J. I., Fassnacht, S. R., Begueria, S., and Latron, J.: Variability of snow depth at
740 the plot scale: implications for mean depth estimation and sampling strategies, 2011. 2011.

741 López-Moreno, J. I., Revuelto, J., Fassnacht, S. R., Azorín-Molina, C., Vicente-Serrano, S. M.,
742 Morán-Tejeda, E., and Sexstone, G. A.: Snowpack variability across various spatio-temporal
743 resolutions, *Hydrological Processes*, doi: 10.1002/hyp.10245, 2014. n/a-n/a, 2014.

744 Luce, C. H., Tarboton, D. G., and Cooley, K. R.: The influence of the spatial distribution of snow
745 on basin-averaged snowmelt, *Hydrological Processes*, 12, 1671-1683, 1998.

746 Lundquist, J. D. and Dettinger, M. D.: How snowpack heterogeneity affects diurnal streamflow
747 timing, *Water Resources Research*, 41, W05007, 2005.

747 Matthews, H. D., Eby, M., Ewen, T., Friedlingstein, P., and Hawkins, B. J.: What determines the
748 magnitude of carbon cycle-climate feedbacks?, *Global Biogeochemical Cycles*, 21, GB2012,
749 2007a.

750 Matthews, H. D., Eby, M., Ewen, T., Friedlingstein, P., and Hawkins, B. J.: What determines the
751 magnitude of carbon cycle-climate feedbacks?, *Global Biogeochemical Cycles*, 21, n/a-n/a,
752 2007b.

753 Matthews, H. D., Weaver, A. J., and Meissner, K. J.: Terrestrial Carbon Cycle Dynamics under
754 Recent and Future Climate Change, *Journal of Climate*, 18, 1609-1628, 2005.

755 McFadden, J. P., Chapin, F. S., and Hollinger, D. Y.: Subgrid-scale variability in the surface
756 energy balance of arctic tundra, *Journal of Geophysical Research: Atmospheres*, 103, 28947-
757 28961, 1998.

758 McGuire, A. D., Clein, J. S., Melillo, J. M., Kicklighter, D. W., Meier, R. A., Vorosmarty, C. J.,
759 and Serreze, M. C.: Modelling carbon responses of tundra ecosystems to historical and projected
760 climate: sensitivity of pan-Arctic carbon storage to temporal and spatial variation in climate,
761 *Global Change Biology*, 6, 141-159, 2000.

762 Mefford, T. K., Bieniulis, M., Halter, B., and Peterson, J.: *Meteorological Measurements*, 17 pp.,
763 1996.

764 Miller, P. C., Stoner, W. A., and Tieszen, L. L.: A Model of Stand Photosynthesis for the Wet
765 Meadow Tundra at Barrow, Alaska, *Ecology*, 57, 411-430, 1976.

766 Montaldo, N. and Albertson, J. D.: Temporal dynamics of soil moisture variability: 2.
767 Implications for land surface models, *Water Resources Research*, 39, n/a-n/a, 2003.

768 Morgner, E., Elberling, B., Strebel, D., and Cooper, E. J.: The importance of winter in annual
769 ecosystem respiration in the High Arctic: effects of snow depth in two vegetation types, *Polar*
770 *Research*, 29, 58-74, 2010.

771 Nobrega, S. and Grogan, P.: Deeper Snow Enhances Winter Respiration from Both Plant-
772 associated and Bulk Soil Carbon Pools in Birch Hummock Tundra, *Ecosystems*, 10, 419-431,
773 2007.

774 Oberbauer, S. F., Tenhunen, J. D., and Reynolds, J. F.: Environmental Effects on CO₂ Efflux
775 from Water Track and Tussock Tundra in Arctic Alaska, U.S.A, *Arctic and Alpine Research*, 23,
776 162-169, 1991.

777 Oechel, W. C., Hastings, S. J., Vourlitis, G., Jenkins, M., Riechers, G., and Grulke, N.: Recent
778 change of Arctic tundra ecosystems from a net carbon dioxide sink to a source, *Nature*, 361, 520-
779 523, 1993.

780 Oleson, K. W., D.M. Lawrence, G.B. Bonan, B. Drewniak, M. Huang, C.D. Koven, S. Levis, F.
781 Li, W.J. Riley, Z.M. Subin, S.C. Swenson, P.E. Thornton, A. Bozbiyik, R. Fisher, E. Kluzek, J.-
782 F. Lamarque, P.J. Lawrence, L.R. Leung, W. Lipscomb, S. Muszala, D.M. Ricciuto, W. Sacks,
783 Y. Sun, J. Tang, Z.-L. Yang: Technical Description of version 4.5 of the Community Land
784 Model (CLM), National Center for Atmospheric Research, Boulder, CO, 422 pp., 2013a.

785 Oleson, K. W., D.M. Lawrence, G.B. Bonan, B. Drewniak, M. Huang, C.D. Koven, S. Levis, F.
786 Li, W.J. Riley, Z.M. Subin, S.C. Swenson, P.E. Thornton, A. Bozbiyik, R. Fisher, E. Kluzek, J.-
787 F. Lamarque, P.J. Lawrence, L.R. Leung, W. Lipscomb, S. Muszala, D.M. Ricciuto, W. Sacks,
788 Y. Sun, J. Tang, Z.-L. Yang: Technical Description of version 4.5 of the Community Land
789 Model (CLM), National Center for Atmospheric Research, Boulder, CO, 2013b.

790 Pau, G. S. H., Bisht, G., and Riley, W. J.: A reduced-order modeling approach to represent
791 subgrid-scale hydrological dynamics for land-surface simulations: application in a polygonal
792 tundra landscape, *Geosci. Model Dev.*, 7, 2091-2105, 2014.

793 Randerson, J. T., Lindsay, K., Munoz, E., Fu, W., Moore, J. K., Hoffman, F. M., Mahowald, N.
794 M., and Doney, S. C.: Multicentury changes in ocean and land contributions to the climate-
795 carbon feedback, *Global Biogeochemical Cycles*, 29, 744-759, 2015.

796 Rogers, M. C., Sullivan, P. F., and Welker, J. M.: Evidence of Nonlinearity in the Response of
797 Net Ecosystem CO₂ Exchange to Increasing Levels of Winter Snow Depth in the High Arctic of
798 Northwest Greenland, *Arctic, Antarctic, and Alpine Research*, 43, 95-106, 2011.

799 Rohrbough, J. A., Davis, D. R., and Bales, R. C.: Spatial variability of snow chemistry in an
300 alpine snowpack, southern Wyoming, *Water Resources Research*, 39, 1190, 2003.

301 Schaefer, K., Zhang, T., Bruhwiler, L., and Barrett, A. P.: Amount and timing of permafrost
302 carbon release in response to climate warming, *Tellus B*, 63, 165-180, 2011.

303 Schimel, J. P., Bilbrough, C., and Welker, J. M.: Increased snow depth affects microbial activity
304 and nitrogen mineralization in two Arctic tundra communities, *Soil Biology and Biochemistry*,
305 36, 217-227, 2004.

306 Schuur, E. A. G. and Abbott, B.: Climate change: High risk of permafrost thaw, *Nature*, 480, 32-
307 33, 2011.

308 Schuur, E. A. G., Bockheim, J., Canadell, J. G., Euskirchen, E., Field, C. B., Goryachkin, S. V.,
309 Hagemann, S., Kuhry, P., Lafleur, P. M., Lee, H., Mazhitova, G., Nelson, F. E., Rinke, A.,
310 Romanovsky, V. E., Shiklomanov, N., Tarnocai, C., Venevsky, S., Vogel, J. G., and Zimov, S.
311 A.: Vulnerability of Permafrost Carbon to Climate Change: Implications for the Global Carbon
312 Cycle, *BioScience*, 58, 701-714, 2008.

313 Seppala, M., Gray, J., and Ricard, J.: Development of low-centred ice-wedge polygons in the
314 northernmost Ungava Peninsular, Québec, Canada, *Boreas*, 20, 259-285, 1991.

315 Sexstone, G. A. and Fassnacht, S. R.: What drives basin scale spatial variability of snowpack
316 properties in northern Colorado?, *The Cryosphere*, 8, 329-344, 2014.

317 Sitch, S., Huntingford, C., Gedney, N., Levy, P. E., Lomas, M., Piao, S. L., Betts, R., Ciais, P.,
318 Cox, P., Friedlingstein, P., Jones, C. D., Prentice, I. C., and Woodward, F. I.: Evaluation of the
319 terrestrial carbon cycle, future plant geography and climate-carbon cycle feedbacks using five
320 Dynamic Global Vegetation Models (DGVMs), *Global Change Biology*, 14, 2015-2039, 2008.

321 Smith, L. C., Sheng, Y., MacDonald, G. M., and Hinzman, L. D.: Disappearing Arctic Lakes,
322 *Science*, 308, 1429-1429, 2005.

323 Smith, M. B., Koren, V., Reed, S., Zhang, Z., Zhang, Y., Moreda, F., Cui, Z., Mizukami, N.,
324 Anderson, E. A., and Cosgrove, B. A.: The distributed model intercomparison project – Phase 2:
325 Motivation and design of the Oklahoma experiments, *Journal of Hydrology*, 418, 3-16, 2012.

326 Smith, N. V., Saatchi, S. S., and Randerson, J. T.: Trends in high northern latitude soil freeze and
327 thaw cycles from 1988 to 2002, *Journal of Geophysical Research: Atmospheres*, 109, D12101,
328 2004.

329 Sturm, M., Douglas, T., Racine, C., and Liston, G. E.: Changing snow and shrub conditions
330 affect albedo with global implications, *Journal of Geophysical Research: Biogeosciences*, 110,
331 G01004, 2005.

332 Sturm, M., Racine, C., and Tape, K.: Increasing shrub abundance in the Arctic, *Nature*, 411, 546,
333 2001.

334 Sullivan, P.: Snow distribution, soil temperature and late winter CO₂ efflux from soils near the
335 Arctic treeline in northwest Alaska, *Biogeochemistry*, 99, 65-77, 2010.

336 Swenson, S. C. and Lawrence, D. M.: A new fractional snow-covered area parameterization for
337 the Community Land Model and its effect on the surface energy balance, *Journal of Geophysical*
338 *Research: Atmospheres*, 117, n/a-n/a, 2012.

339 Tang, J. and Riley, W. J.: Large uncertainty in ecosystem carbon dynamics resulting from
340 ambiguous numerical coupling of carbon and nitrogen biogeochemistry: A demonstration with
341 the ACME land model, *Biogeosciences Discuss.*, 2016, 1-27, 2016.

342 Tape, K. E. N., Sturm, M., and Racine, C.: The evidence for shrub expansion in Northern Alaska
343 and the Pan-Arctic, *Global Change Biology*, 12, 686-702, 2006.

344 Tarnocai, C., Canadell, J. G., Schuur, E. A. G., Kuhry, P., Mazhitova, G., and Zimov, S.: Soil
345 organic carbon pools in the northern circumpolar permafrost region, *Global Biogeochemical*
346 *Cycles*, 23, GB2023, 2009.

347 Thompson, S. L., Govindasamy, B., Mirin, A., Caldeira, K., Delire, C., Milovich, J., Wickett,
348 M., and Erickson, D.: Quantifying the effects of CO₂-fertilized vegetation on future global
349 climate and carbon dynamics, *Geophysical Research Letters*, 31, L23211, 2004.

350 Wadham, J. L., Hallam, K. R., Hawkins, J., and O'Connor, A.: Enhancement of snowpack
351 inorganic nitrogen by aerosol debris, *Tellus B*, 58, 229-241, 2006.

352 Wahren, C. H. A., Walker, M. D., and Bret-Harte, M. S.: Vegetation responses in Alaskan arctic
353 tundra after 8 years of a summer warming and winter snow manipulation experiment, *Global*
354 *Change Biology*, 11, 537-552, 2005.

355 Wainwright, H. M., Dafflon, B., Smith, L. J., Hahn, M. S., Curtis, J. B., Wu, Y., Ulrich, C.,
356 Peterson, J. E., Torn, M. S., and Hubbard, S. S.: Identifying multiscale zonation and assessing
357 the relative importance of polygon geomorphology on carbon fluxes in an Arctic tundra
358 ecosystem, *Journal of Geophysical Research: Biogeosciences*, 120, 788-808, 2015.

359 Walker, D. A., Raynolds, M. K., Daniëls, F. J. A., Einarsson, E., Elvebakk, A., Gould, W. A.,
360 Katenin, A. E., Kholod, S. S., Markon, C. J., Melnikov, E. S., Moskalenko, N. G., Talbot, S. S.,
361 Yurtsev, B. A., and The other members of the, C. T.: The Circumpolar Arctic vegetation map,
362 *Journal of Vegetation Science*, 16, 267-282, 2005.

363 Warscher, M., Strasser, U., Kraller, G., Marke, T., Franz, H., and Kunstmann, H.: Performance
364 of complex snow cover descriptions in a distributed hydrological model system: A case study for
365 the high Alpine terrain of the Berchtesgaden Alps, *Water Resources Research*, 49, 2619-2637,
366 2013.

367 Welker, J. M., Fahnestock, J. T., and Jones, M. H.: Annual CO₂ Flux in Dry and Moist Arctic
368 Tundra: Field Responses to Increases in Summer Temperatures and Winter Snow Depth,
369 *Climatic Change*, 44, 139-150, 2000.

370 Wiggins, I. L.: The distribution of vascular plants on polygonal ground near Point Barrow,
371 Alaska, Stanford University Contributions of the Dudley Herbarium, 4, 41-52, 1951.

372 Williams, M. W., Hood, E., and Caine, N.: Role of organic nitrogen in the nitrogen cycle of a
373 high-elevation catchment, Colorado Front Range, Water Resources Research, 37, 2569-2581,
374 2001.

375 Williams, T. and Flanagan, L.: Effect of changes in water content on photosynthesis,
376 transpiration and discrimination against $^{13}\text{CO}_2$ and $\text{C}^{18}\text{O}^{16}\text{O}$ in Pleurozium and Sphagnum,
377 Oecologia, 108, 38-46, 1996.

378 Wu, Y., Hubbard, S. S., Ulrich, C., and Wulschleger, S. D.: Remote Monitoring of Freeze–
379 Thaw Transitions in Arctic Soils Using the Complex Resistivity Method, gsvadzone, 2013. 2013.

380 Xu, X., Riley, W. J., Koven, C. D., Billesbach, D. P., Chang, R. Y. W., Commane, R.,
381 Euskirchen, E. S., Hartery, S., Harazono, Y., Iwata, H., McDonald, K. C., Miller, C. E., Oechel,
382 W. C., Poulter, B., Raz-Yaseef, N., Sweeney, C., Torn, M., Wofsy, S. C., Zhang, Z., and Zona,
383 D.: A multi-scale comparison of modeled and observed seasonal methane emissions in northern
384 wetlands, Biogeosciences, 13, 5043-5056, 2016.

385 Zeng, N., Qian, H., Munoz, E., and Iacono, R.: How strong is carbon cycle-climate feedback
386 under global warming?, Geophysical Research Letters, 31, L20203, 2004.

387 Zeng, X. and Decker, M.: Improving the Numerical Solution of Soil Moisture–Based Richards
388 Equation for Land Models with a Deep or Shallow Water Table, Journal of Hydrometeorology,
389 10, 308-319, 2009.

390 Zhu, Q., Iversen, C. M., Riley, W. J., Slette, I. J., and Vander Stel, H. M.: Root traits explain
391 observed tundra vegetation nitrogen uptake patterns: Implications for trait-based land models,
392 Journal of Geophysical Research: Biogeosciences, 121, 3101-3112, 2016.

393 Zhu, Q. and Riley, W. J.: Improved modelling of soil nitrogen losses, Nature Clim. Change, 5,
394 705-706, 2015.

395 Zona, D., Lipson, D. A., Zulueta, R. C., Oberbauer, S. F., and Oechel, W. C.: Microtopographic
396 controls on ecosystem functioning in the Arctic Coastal Plain, Journal of Geophysical Research:
397 Biogeosciences, 116, G00I08, 2011.

398